Lifetimes and Spatio-Temporal Response of Protein Crystals in Intense X-ray Microbeams

Matthew A. Warkentin[ab], Hakan Atakisi[c], Jesse B. Hopkins[d], Donald Walko[e] and Robert E. Thorne[c]*

[a]Physics Department, Cornell University, Clark Hall, Ithaca, NY, 14853, USA

[b] Rubota Corporation, 1260 NW Naito Pkwy #609, Portland, OR, 97209, USA

[c]Physics Department, Cornell University, Ithaca, NY, 14853, USA

[d] Cornell High Energy Synchrotron Source, Ithaca, NY, 14853, United States

[e]Advanced Photon Source, Argonne National Laboratory, 9700 S. Cass Ave., Argonne, IL, 60439, USA

Correspondence email: ret6@cornell.edu

Synopsis The complex evolution of diffracted intensities from protein crystals during irradiation by intense Gaussian X-ray microbeams is measured and analysed. The analysis explains non-exponential intensity decays without invoking sequential damage models, yields a revised metric to quantify the crystal's damage state after a given irradiation time, explains previous observations of a damage "lag" phase, and shows how ultra-intense X-ray microbeams allow the data collected per crystal at and near room temperature to be increased.

Abstract Serial synchrotron-based crystallography using intense microfocused X-ray beams, fast framing detectors, and protein microcrystals held at 300 K promises to expand the range of accessible structural targets and increase overall structure pipeline throughputs. To explore the nature and consequences of X-ray radiation damage under microbeam illumination, the time-, dose-, and temperature-dependent evolution of crystal diffraction have been measured with maximum dose rates of 50 MGy/s. At all temperatures and dose rates, the integrated diffraction intensity for fixed crystal orientation shows non-exponential decays with dose. Non-exponential decays are a consequence of nonuniform illumination and the resulting spatial evolution of diffracted intensity within the illuminated crystal volume. To quantify radiation damage lifetimes and the damage state of diffracting crystal regions, we define a revised diffraction-weighted dose (DWD), and show that for Gaussian beams the DWD becomes nearly independent of actual dose at large doses. An apparent delayed onset of radiation damage seen in some intensity-dose curves is in fact a consequence of damage. Intensity fluctuations at high dose rates may arise from impulsive release of gaseous damage products. Accounting for these effects, data collection at the highest dose rates increases crystal radiation lifetimes near 300 K (but not

at 100 K) by a factor of ~1.5-2 compared to those observed at conventional dose rates. Improved quantification and modelling of the complex spatio-temporal evolution of protein microcrystal diffraction in intense microbeams will enable more efficient data collection, and will be essential in improving the accuracy of structure factors and structural models.

Keywords: protein crystallography; radiation damage; serial crystallography; microcrystallography

1. Introduction

The overwhelming majority of biomacromolecular structures have been and will continue to be determined by X-ray crystallography. Increasing synchrotron source brilliance allows X-ray flux to be concentrated into smaller and smaller beams. This in turn allows data collection from smaller and smaller crystals and longstanding challenges in growing large crystals of important targets (e.g., membrane proteins, large complexes) to be bypassed. Motivated by the success of serial femtosecond crystallography using X-ray free-electron lasers (XFELs), methods for synchrotron-based serial microcrystallography are being developed (Roessler *et al.*, 2013; Stellato *et al.*, 2014; Heymann *et al.*, 2014; Coquelle *et al.*, 2015; Botha *et al.*, 2015; Mueller *et al.*, 2015; Lyubimov *et al.*, 2015), combining ultra-intense microfocused beams, multiple crystal holders or continuous crystal feed systems, and fast framing detectors with computational tools for indexing, merging, and modelling diffraction data from large numbers of crystals (Kabsch, 2010; Ginn *et al.*, 2016; Gildea *et al.*, 2014; White *et al.*, 2016; Ayyer *et al.*, 2015). To maximize crystal lifetimes, nearly all protein crystallography is performed on crystals cooled to T=100 K. However, at 300 K crystals have much smaller mosaicities and are more likely to be isomorphous (Kriminski *et al.*, 2002; Malkin & Thorne, 2004; Pflugrath, 2004; Juers & Matthews, 2004; Farley *et al.*, 2014). Recently developed computational methods (Lang *et al.*, 2010; Van Den Bedem *et al.*, 2009; Fenwick *et al.*, 2014) for analysing low-density features in electron density maps and experimental protocols for 300 K and variable temperature data collection (Warkentin & Thorne, 2010*b*) are beginning to reveal a wealth of information about a protein's conformational ensemble that is corrupted on cooling to cryogenic temperatures (Fraser *et al.*, 2009; Keedy *et al.*, 2015).

These trends have made understanding, minimizing, and modelling damage caused by the illuminating X-rays increasingly important. Inelastic X-ray photon scattering and photoelectron ejection lead to a cascade of chemical and structural processes, from generation of secondary electrons and free radicals, reduction of metal centers, breaking of chemical bonds, and formation of hydrogen gas, to conformational relaxations and local unfolding, molecular displacements and lattice distortions, and plastic failure (Holton, 2009; Garman, 2010; Warkentin *et al.*, 2013). These processes change the protein's average structure within the crystal, introduce molecule-to-molecule deviations from that

average structure, and cause spatial variations in the local lattice spacing and orientation. In X-ray diffraction, these changes manifest as changes in the intensities, shapes, and positions of the Bragg peaks with dose, especially at large scattering angles, and in increased diffuse scattering.

Previous radiation damage studies on protein crystals using large (50-400 μm) X-ray beams and large crystals have established that damage depends on dose (measured in Grays (Gy) = J/kg), determined by the incident photon energy and flux density and the crystal composition; that the integrated intensity in Bragg peaks decays approximately exponentially with dose (Holton, 2009; Garman, 2010); and that the rate of radiation damage increases by a factor of ~30-50 between 100 K and 300 K, with substantial protein-to-protein variation (Warkentin *et al.*, 2014).

Less is known about the response of protein crystals to intense X-ray microbeams generated using synchrotrons (Smith *et al.*, 2012). These beams typically have Gaussian intensity profiles with widths of a few to a few tens of micrometers and generate spatially nonuniform damage. At higher X-ray energies, photoelectrons can deposit their energy micrometers from the absorption site (Nave & Hill, 2005; Sanishvili *et al.*, 2011; Finfrock *et al.*, 2013), so that beam and damage profiles may differ. Intense beams degrade diffraction rapidly, so data must be collected using fast framing detectors, and time- as well as dose-dependent effects may manifest (Warkentin *et al.*, 2012; Owen *et al.*, 2012; Warkentin *et al.*, 2013; Owen *et al.*, 2014). Consequently, standard assumptions about the effects of irradiation and induced disorder on diffracted intensities may become invalid, additional errors may be introduced into measured structure factors, and the relatively poor R factors of refined protein structures (Holton *et al.*, 2014) may become even worse. Here we explore the complex evolution of diffracted intensities from protein crystals illuminated by intense X-ray microbeams, and show how these can be interpreted in terms of the spatiotemporal evolution of radiation damage. These results have important consequences for optimizing data collection, for extracting structure factors from measured intensities, and for studying the underlying mechanisms of radiation damage.

2. Methods

Data collection protocols are critical to interpreting results of radiation damage studies, so we first give a brief overview of our methods, described in more detail below and in the Supporting Information (SI). To assess damage by X-ray microbeams, a large and highly redundant data set of ~50,000 diffraction frames was acquired from ~1300 independent positions on 26 crystals of lysozyme and thaumatin at temperatures of 100 K, 260 K, and 300 K. Crystals of roughly 100-600 μm size were illuminated with a Gaussian profile X-ray microbeam (Fig. S1) with a full width at half maximum (FWHM) of 2.4 × 5.1 μm and delivering peak (at beam center) and nominal (average within the FWHM) dose rates of ~49 and ~35 MGy/s, respectively, a factor ~10^3 larger than in conventional crystallographic practice. To ascertain the dose rate dependence of damage, attenuators were used to

reduce dose rate by factors of up to ~10^3. Each crystal was held in fixed orientation and diffraction frames vs dose at different dose rates were collected from an array of positions (Fig. S2). Bragg peak intensities in each frame were integrated, and this integrated intensity was plotted versus dose to yield an intensity-dose relation or "dose curve" at each position and dose rate.

2.1. Sample preparation

Tetragonal thaumatin and tetragonal lysozyme crystals were grown by hanging drop vapor diffusion using standard recipes (SI S1). Crystals for measurements at 260 K and 300 K were transferred to a high viscosity oil to remove external solvent and then harvested and mounted for data collection using microfabricated polyimide or nylon cryoloops. The oil thickness was typically 50 to 100 μm, and was sufficient to prevent any dehydration (as monitored through unit cell parameters) during the ~15-30 minutes each crystal was examined. As an additional check, some oil-covered crystals were also mounted in polyimide capillaries, and gave similar results. Crystals for measurements at 100 K were first soaked in a 20% w/v glycerol solution and then transferred to a drop of low viscosity oil to remove external solvent before mounting and insertion in a cold nitrogen gas stream.

2.2. Beamline setup and beam characteristics

X-ray diffraction data was collected at the D-hutch of Argonne X-ray Science Division beamline 7-ID at the Advanced Photon Source. A 10 keV X-ray beam was focused using two K-B mirrors onto a fluorescent screen at the sample position. The beam profile was measured by scanning the edge of a gallium arsenide wafer in *x*, *y*, and *z*, measuring the transmitted intensity, and fitting the resulting curve with an error function to extract the FWHM. An example beam image and profile determined in this way are shown in Fig. S1. Beam position and size were continuously monitored and were exceptionally stable, requiring only minor adjustments. Measured beam FWHM values were 2.5 μm (v) by 5.1 μm (h), and the focused beam's divergence at the sample was approximately 0.07° (v) by 0.13° (h). The incident flux was monitored with a calibrated 7 cm ion chamber located 0.64 m downstream of the sample. Corrected for air absorption, the flux at the sample position was 1.2×10^{12} photons/s.

2.3. Dose rate calculations

Using the measured photon flux and FWHM, the peak flux density within the FWHM was ~1.2×10^{17} photons/(mm^2 s), respectively. Corresponding nominal (average within the FWHM) and peak dose rates calculated using RADDOSE 3D (Zeldin, Gerstel *et al.*, 2013) were 36 and 49 MGy/s for thaumatin and 33 and 45 MGy/s for lysozyme. Calibrated aluminum attenuators reduced the incident flux at the sample (determined from air-absorption-corrected ion chamber measurements) by factors of ~11, 46, 377 and 847, giving nominal dose rates for thaumatin of ~3.3, 0.78, 0.095, and 0.042 MGy/s. These dose rate estimates do not include the effects of finite photoelectron mean free paths (SI S5) (Finfrock

et al., 2013; Nave & Hill, 2005; Sanishvili *et al.*, 2011) or fluorescence. These effects are independent of dose rate and are small for the beam size used here.

2.4. Diffraction data collection

X-ray diffraction data were collected using a PILATUS3 300K detector having a maximum frame rate of 500 Hz. The detector was mounted with its lower edge just above the direct beam, and with its face tilted (at ~22°) so that the detector's center was normal to the diffracted beam direction at that position. For data acquisition with the unattenuated beam, the full 500 Hz frame rate was used; for attenuated beams, the exposure time per frame was increased by the attenuation factor so that frames acquired with different attenuation settings were comparably exposed. Counts per pixel per frame in the brightest diffraction peaks were typically <10000, giving a dead-time-corrected error in the 1 ms exposure at the highest frame of less than 10% (SI S9). At a given position on a crystal, diffraction patterns were acquired at the attenuation-dependent frame rate for a total exposure time that gave a significant reduction — by a factor of ~3 at 260 K and 300 K — in the crystal's Bragg diffraction. Between 5 and 35 diffraction time series were acquired from each crystal at each of the five attenuation settings by stepping the crystal through the beam in 20 μm steps. The crystal orientation was fixed, ensuring that a fixed crystal volume was illuminated throughout each frame series.

2.5. Data processing

The ~50,000 individual diffraction frames were processed using DISTL (Zhang *et al.*, 2006; Sauter, 2010), and separately using XDS (Kabsch, 2010) to extract Bragg peak positions and intensities. The frames were all "stills" (i.e., recorded with zero oscillation) and captured roughly 40% of the full diffraction pattern. At 260 K and 300 K thaumatin crystal mosaicities are typically very small (<0.01°). Each frame thus had at most a few hundred well-exposed peaks. Attempts to index the frames were often unsuccessful, and parameter choices that allowed successful indexing did not give sensible mosaicity values. To quantify radiation damage, an integrated intensity for each frame was calculated using DISTL by summing the integrated spot intensities in pixel ADC units above local background. As a check on these results, a measure of integrated intensity for each frame was calculated by summing peak I/σ values in XDS's SPOT output. These two integrated intensities were then plotted versus frame number ($\propto$ dose) to obtain a "dose curve". Similar metrics of integrated intensity have been used in previous high-dose-rate studies of radiation damage (Owen *et al.*, 2012, 2014). To assist in interpreting dose curves, the DISTL and XDS-generated intensities of each individual diffraction peak versus frame number for all ~1300 dose series were plotted and manually inspected. All data and figures presented here are based on analysis using DISTL, but qualitatively and quantitively similar results were obtained using XDS (SI S14).

3. Results and Discussion

3.1. Integrated intensity versus dose: Nonexponential decays and a "lag phase"

Figures 1 and S5 show representative plots of integrated intensity versus dose for five different dose rates at 300 K and 260 K. At all temperatures, the dose curves have a roughly exponential dependence on dose (dashed lines) until the integrated intensity has dropped to roughly half its initial value (at a dose called the half-dose $D_{1/2}$). However, at larger doses the curves deviate above the initial exponential trend. This deviation is observed at all dose rates for all crystals of lysozyme and thaumatin at all temperatures. Intensity versus dose curves with comparable shapes and initial slopes are obtained when integrating only the 10, 25, 50, and 100 brightest peaks in each frame set, indicating that deviations from exponential behavior are not a consequence of background subtraction (except perhaps at very large doses where the integrated intensity becomes very small). Attempts to force exponential behavior by adjusting background subtraction give decays with dose a factor of ~3 more rapid than in previous measurements.

Not all measured dose curves exhibit an initial exponential decay. As shown in Fig. 2, roughly 5% of 683 lysozyme dose curves and 25% of 627 thaumatin dose curves show an initial plateau or near plateau. Similar behavior at dose rates above 1 MGy/s has been reported (Owen *et al.*, 2012, 2014) and the apparent delay in intensity decay has been described as a "lag phase." These initial plateaus are observed here at all dose rates and temperatures. Their width *in time* varies according to dose rate by a factor of ~10^3 at each temperature, but their width *in dose* is roughly consistent (Owen *et al.*, 2014), generally ~1/4 to 1/2 the half-dose $D_{1/2}$. Some crystals — each with a different orientation — yield far more dose curves with plateaus than others. Of the 7 thaumatin crystals examined at 260 K, one shows plateaus or small initial slopes in all 84 of its dose curves, whereas another shows plateaus or small initial slopes in only 5 of its 51 dose curves.

3.2. Bragg peak intensities versus dose

Plots of individual Bragg peak intensities versus dose aid in interpreting integrated intensity plots, allowing artefacts due to sample motion and spurious diffraction peaks from, e.g., salt to be identified. These plots also provide insight into the origin of the plateaus in Fig. 2 (top). As illustrated in Fig. 2 (bottom), in *every* case in which the integrated intensity versus dose exhibits an initial plateau or near plateau, a few to several intense Bragg peaks have intensities that initially increase rapidly or show plateaus with dose. The eventual radiation-damage-induced decay of these peaks occurs at doses that roughly match the width of the integrated intensity plateau. When only the brightest 10 or 25 peaks in each frame are integrated, the integrated intensity can show a significant initial rise with dose before decaying at larger doses. Similarly, in every case where plateaus vs dose are not observed, at most one or two intense peaks show initial increases. These trends are not an artefact of background subtraction and integration, and are clearly visible in the original diffraction frames.

3.3. Intensity fluctuations at high dose and frame rates

As shown in SI-Fig. S7, at 260 K and especially 300 K, integrated intensity versus dose curves acquired at the highest dose rate and detector frame rate (500 Hz) consistently show fluctuations — where the integrated intensity rises for 1 or 2 frames before dropping back down to the overall trend — that are brief in both dose and time. At the second highest dose rate and frame rate (83 Hz), smaller jumps are observed, and at the lowest dose and frame rate (1.2 Hz) the dose curves are generally smooth. At all dose rates fluctuations are observed only at doses comparable to or beyond the half-dose $D_{1/2}$, and the typical separation in dose between individual fluctuations in a given dose curve is of the same order as the half dose. No such fluctuations are observed at any dose rate for either protein at 100 K, although that data do not extend beyond the (large) half doses at that temperature.

3.4. Temperature and dose-rate dependent half doses

Figure 3 and Table S1 give the measured nominal half doses $D_{1/2}$ versus nominal dose rate and temperature for lysozyme and thaumatin. Half doses were obtained from an exponential fit to the initial decay of each dose curve, down to where the intensity dropped to roughly one-half of its initial value. Dose curves exhibiting initial plateaus were excluded from this analysis, although fits to those curves over an equivalent dose range that excluded the initial plateau yielded quantitatively similar half-doses to those in Fig. 3. At T=100 K, the half-dose is independent of dose rate over the entire dose rate range. At 260 K and 300 K, a clear dose-rate dependence is observed for both proteins. Using the unattenuated beam with a nominal dose rate of 33-36 MGy/s increases the half dose by factors of ~1.5-2 at 260 K and 300 K relative to data collected at dose rates of less than 100 kGy/s. This half-dose increase is real, and is not a detector artefact caused by large incident photon fluxes per pixel (SI S9). At a nominal dose rate of ~36 MGy/s, the half dose is reached in ~6 ms at 300 K and in ~10 ms at 260 K. Consequently, some radiation damage can be outrun and the amount of data collected per crystal increased by collecting diffraction data on this time scale.

3.5. Form of the intensity versus dose curves

The observed form of the intensity versus dose curves is a consequence of nonuniform irradiation (SI S12) provided by Gaussian profile microbeams and the resulting “hole burning”. Consider the following model. Let $F(\vec{\ },\ ,\ )$ be the incident flux density (in ph/m^2/s) at crystal position $\vec{\ }$ and time t, and $D(\vec{\ },\ ,\ )$ be the dose (in J/kg) delivered at $\vec{\ }$ from t=0 to t, which depends on the incident flux density, X-ray energy, and crystal composition. Let $S\big(D(\vec{\ },\ ,\ ,$ be the diffracted flux per unit illuminated crystal volume per unit incident flux density at position $\vec{\ }$ and time t (averaged overall all reflections, proportional to the integrated intensity). $S\big(D(\vec{\ },\ ,\ ,$ depends on how the crystal’s

diffracting power at position $\vec{r}$ is reduced by damage caused by the dose $D(\vec{r},t)$. Assume an exponential decay, $S\left(D(\vec{r},t)\right) = \exp\left(-D(\vec{r},t)/D_e\right)$, where the local half-dose (corresponding to the value measured using a uniformly irradiated crystal) is $D_{1/2,\,\mathrm{local}} = D_e \ln(2)$. Further assume that the incident flux density $F(\vec{r})$ is time independent (the beam flux density is constant and the crystal is not rotated or translated) and cylindrically symmetric about the beam center, and that the crystal is thin so that X-ray attenuation along the beam path can be neglected. The total diffracted flux from the sample at time *t* is then

$$\Phi_{diff}(t) = \Delta z \int_0^\infty F(r) S\left(D(r,t)\right) \cdot 2\pi r \cdot dr$$

where Δz is the crystal thickness along the beam and the dose $D(r,t) = ktF(r)$ where *k* is a constant that depends on X-ray energy and sample composition.

Figure 4 (top) shows the resulting diffracted flux, proportional to the integrated intensity measured by the detector, versus normalized dose for a Gaussian profile X-ray beam ,

$$F(r,t) = F_0 \frac{1}{2\pi\sigma^2} e^{-\frac{r^2}{2\sigma^2}},$$

and a top-hat profile beam with the FWHM and same total flux. For the Gaussian beam, the decay with dose is roughly exponential until the diffracted flux (integrated intensity) has decayed to roughly half its initial value, and is then much more gradual than this initial trend would predict. As shown in Figs. 1 and S5, the calculated functional form provides a reasonable fit to integrated intensity versus nominal dose data for all dose rates at all temperatures studied here. Deviations of the fit above the data at large doses / small intensities are most likely due to the decreased diffraction resolution and the increase in effective half-dose with decreasing resolution (Howells *et al.*, 2009), to deviations of the beam shape from a strict Gaussian, and possibly due to errors in background subtraction. The calculated half dose, using the average dose delivered in the beam's FWHM, is $D_{1/2} = 1.66 D_{1/2,\,\mathrm{local}}$, where $D_{1/2,\,\mathrm{local}}$ is the "true", local half dose.

Figure 5 illustrates the origin of the non-exponential form of the calculated and observed dose curves. The incident flux density and dose vary with *r* within the illuminated crystal region. Initially, the diffracted flux per unit illuminated crystal area in Fig. 5 (top) is strongest at *r*=0 and in the strongly illuminated core within the FWHM. However, since the core receives the largest dose rate, it is the most rapidly damaged, and diffraction from it fades most rapidly. Near the half-dose in Fig. 4, the diffracted flux per unit area in Fig. 5 has flattened near *r*=0. At larger average doses radiation damage has burned a "hole" near *r*=0, and the most strongly diffracting regions are at larger radii. Figure 5 (bottom) shows the (circumferentially integrated) diffracted flux per unit radius. The region near *r*=0, despite producing the largest initial flux density, has a small area and contributes little to the total diffracted flux. The peak

flux per unit radius moves from r/σ=1 to larger r as irradiation proceeds, with its shift per unit dose (time) decreasing with increasing dose.

Nonexponential intensity decays with dose or illumination time have been observed in most previous radiation damage studies of protein crystals (Warkentin & Thorne, 2010*a*; Owen *et al.*, 2014; Blake *et al.*, 1962; Hendrikson, 1976; Sliz *et al.*, 2003; Liebschner *et al.*, 2015). When Bragg peak intensities within narrow resolution shells have been plotted versus dose, higher resolution shells deviated from exponential behavior at lower doses. These data have been analysed using models (Blake *et al.*, 1962; Sygusch & Allaire, 1988; Hendrikson, 1976) that consider local dose-dependent transitions between undamaged protein, partially disordered protein, and fully amorphous protein, and that give rise to a locally non-exponential dose response. However, in all experiments the crystals were nonuniformly irradiated due to a nonuniform beam profile and/or due to sample rotations during illumination. With an underlying exponential intensity-dose relation, nonuniform illumination alone can explain the qualitative shape of the observed intensity vs dose curves (SI S12). Resolution dependence of the non-exponential behavior results because the effective local half dose decreases with increasing resolution (Howells *et al.*, 2009). Consequently, the experimental form of the local dose response and its implications for damage mechanisms must be re-evaluated in light of the present analysis.

3.6. Quantifying radiation damage: half doses and average dose state

In routine crystallographic practice, the crystal is rotated instead of fixed, the X-ray beam is often smaller than the crystal, and the crystal volume illuminated by the beam changes substantially with orientation (Zeldin, Gerstel *et al.*, 2013), so that different regions of the crystal receive different doses during data set collection. Consequently, the photons recorded in a given frame will come from crystal regions that have received different doses, are in different damage states, and that differ both in their resolution and in specific structural details due to molecular damage.

A diffraction-weighted dose (denoted here by *DWD**, for reasons to become clear shortly) has been proposed as a better metric of the damage state in such cases of non-uniform irradiation (Zeldin, Brockhauser *et al.*, 2013). *DWD** is defined as

$$DWD^*(t) = \frac{\int_0^t \int_{crystal} D(\vec{r},t')F(\vec{r},t')\,d\vec{r}\,dt'}{\int_0^t \int_{crystal} F(\vec{r},t')\,d\vec{r}\,dt'},$$

where $F(\vec{r},t')$ is the incident flux density and $D(\vec{r},t')$ is the total cumulative dose at *crystal* position $\vec{r}$ at time t'. *DWD** weights the dose delivered to each region of a crystal by the amount of X-ray illumination it receives, assumed to be proportional to its contribution to the measured diffraction. Regions that are weakly or transiently illuminated receive a small dose, and the contribution of their

dose to the *DWD** is down-weighted. For a Gaussian profile X-ray beam and fixed crystal orientation as used here, $F(\vec{r},t,\quad F,\vec{r},$ and $D(\vec{r},t,\quad t\quad F,\vec{r},$, *DWD** is 0.25 times the maximum dose $D_{\max} \propto F(\vec{r}\quad -,$ at beam center, and 0.35 times the average dose delivered in the beam's FWHM. The ratio of *DWD** to $D_{\max}$ is constant, independent of irradiation time. Consequently, plots of integrated diffraction intensity versus *DWD**, $D_{\max}$ or average dose all have the same functional form.

However, *DWD** is in fact an *incident flux density weighted dose*: it assumes that the diffracted flux at time *t* depends only upon the incident flux, and not on the accumulated dose. Consequently, it does not capture the dose state of the crystal regions that are responsible for diffraction at time *t*. For example, suppose a crystal is irradiated by a small square beam for a long time t_1, receiving a large dose D_1 such that the illuminated region ceases diffracting. If the beam is translated by half its width, *DWD** will initially be $D_1 / 2$, even though all diffraction comes from previously unirradiated and thus undamaged crystal.

A true diffraction weighted dose (DWD) can be defined as

$$DWD(t) = \frac{\int_0^t \int_{crystal} D(\vec{r},t,S,\vec{r},t,F,\vec{r},t,d\ r\ dt'}{\int_0^t \int_{crystal} S(\vec{r},t,F,\vec{r},t,d\ r\ dt'},$$

where the denominator gives the total diffracted intensity. The difference between *DWD* and *DWD** is evident in Fig. 5 (bottom), calculated assuming a fixed orientation sample illuminated using a Gaussian profile beam. *DWD** grows linearly with dose. The true *DWD* has an initial roughly linear increase and then bends over, becoming nearly independent of dose at large doses. In other words, the dose that has been received by *those regions of the crystal that dominate diffraction at time t* becomes nearly independent of average dose delivered to the crystal as a whole at large crystal doses. The reason for this surprising behavior is evident from Fig. 5 (bottom): as irradiation proceeds, the strongest diffraction comes from more weakly damaged regions at larger *r* values in the Gaussian profile, and there is much more sample volume per unit *r* at large *r* than at small *r*. When the diffracted intensity has dropped to half of its initial, zero-dose value, *DWD** overestimates the true *DWD* by 35%, and this grows to 77% when the intensity is 30% of its initial value. For general incident X-ray beam profiles and sample irradiation patterns, *DWD* provides a more relevant and lower estimate of the dose state of the sample, and is a key metric for optimizing data collection protocols.

3.7. Origin of anomalous intensity variations and the "lag phase"

Rather than indicating a delayed onset of radiation damage, initial plateaus in integrated intensity versus nominal dose, as in Fig. 2, result from damage-induced redistribution of electron density in reciprocal space. As a crystal is damaged, its unit cell dimensions, the width of its unit cell size distribution, and its mosaicity all increase (Ravelli *et al.*, 2002; Ravelli & McSweeney, 2000; Shimizu

et al., 2007; Rajendran *et al.*, 2011; Garman & Owen, 2006; Coughlan *et al.*, 2016; Holton, 2009; Garman, 2010). In reciprocal space, these changes correspond to radial motion, radial broadening, and axial broadening of reciprocal lattice peaks about q=0. Radiation-induced reciprocal lattice peak broadening and motion can increase the overlap of some reciprocal lattice peaks with the Ewald sphere's surface, initially increasing the corresponding Bragg peak intensity, before the peak intensities decay due to the overall decay of crystal diffracting power (described by the B factor); for peaks initially located on the Ewald sphere's surface, these effects cause more rapid intensity decay. The fraction of reciprocal lattice peaks suitably positioned to generate initial Bragg peak brightening varies with crystal orientation, and in some orientations is sufficient to generate integrated intensity plateaus. The systematics of this Bragg peak brightening allow it to be distinguished from intensity changes due to site-specific damage (SI S10).

Generation of integrated intensity plateaus by this mechanism requires that the rate of mosaicity and/or cell size distribution broadening with dose be "larger" in some sense than the rate of overall loss of crystal diffracting power. Plateaus may be more prevalent for crystals with small initial mosaicities, illuminated by at most weakly diverging X-ray beams, held in fixed orientation during irradiation – the conditions most likely to prevail during serial synchrotron crystallography. Plateaus may be particularly acute when the beam is smaller than the crystal, as undamaged surrounding crystal regions then constrain irradiation-induced unit cell expansion and may lead to fracturing and increased mosaic broadening. The underlying rapid and non-monotonic evolution of individual Bragg peak intensities with dose (corresponding to a dose-dependent reflection partiality) will complicate estimation of structure factors, especially when crystal diffraction is weak so that peak intensity evolution with dose cannot be reliably recorded.

3.8. Origin of intensity fluctuations in high dose- and frame-rate data collection

The salient features of the integrated intensity fluctuations with dose shown in Figs. S7 and S8 are (1) they appear only after the sample has received a substantial dose, of the order of the nominal half dose; (2) they have largest amplitude for data collected with the highest dose rate and shortest frame period; (3) they always involve a transient increase in intensity, but do not rise to the zero-dose intensity; and (4) most or all diffraction peaks in a given frame fluctuate in the same way. The fluctuations are not observed at low doses, regardless of dose rate, and are not obviously present in data collected at low dose and frame rates. (1) indicates that these fluctuations are associated with radiation damage, and that a minimum dose / amount of damage is required. (2) suggests that the timescale for the fluctuations is short – on the order of milliseconds. (3) and (4) suggest that they arise from a small (~200 nm or 0.03°) motion of the crystal that brings a small volume of less exposed and less damaged crystal into the beam.

Intensity fluctuations may arise from crystal and mounting loop "quakes" in response gas bubble formation and bursting. Irradiation cleaves off H atoms (Meents *et al.*, 2010; Leapman & Sun, 1995) that, at sufficiently high temperature, can recombine to form H_2. When crystals that have received a

large dose at 100 K (where free radicals and hydrogen are immobile) are warmed to 300 K by blocking the cold gas stream, rapid radical diffusion, reaction, and H_2 production can lead to gas bubbling that destroys the crystal in a few seconds (Garman, 2010). When room temperature crystals are irradiated at ~35 MGy/s, large doses are delivered in tens of milliseconds, the hydrogen concentration in the illuminated volume rises rapidly, and bubbles may nucleate, grow, and burst, delivering impulses to the crystal and its mount that transiently bring less exposed crystal regions into the beam. Intensity fluctuations may also arise from crystal fracturing that relieves stress from damage-induced expansion of the irradiated volume. Both bubble growth/bursting and fracturing may generate significant uncertainties in structure factor estimates based on microbeam data from weakly diffracting microcrystals.

3.9. Outrunning radiation damage using intense microbeams

While the timescales for the chemical processes involved in radiation damage to protein crystals at and near room temperature are microseconds and shorter, the timescales for structural relaxations in response to chemical damage – including side chain rotations, main chain displacements and unfolding, molecular displacements and rotations within the unit cell, and the longer range lattice distortions responsible for the increase in mosaicity and unit cell volume - may be much longer, especially for motions involving many atoms that may have a much larger effect on diffracted intensities than, e.g., the breaking of bonds that precipitate the motions (Warkentin *et al.*, 2013, 2014). At room temperature, the rate of diffraction spot fading with dose varies between proteins by a factor of 10 or more, even though the extent of chemical damage per unit dose should be similar, suggesting the importance of structural relaxations (Warkentin *et al.*, 2014).

Several recent synchrotron-based experiments (Leiros *et al.*, 2006; Southworth-Davies *et al.*, 2007; Warkentin *et al.*, 2012; Owen *et al.*, 2012, 2014) have probed the dose-rate dependence of radiation damage, and the feasibility of outrunning some fraction of damage by using intense microbeams and fast data collection. The results have been inconclusive. Reported increases in crystal lifetimes using large dose rates have varied substantially, and detector undercounting when photon fluxes/pixel are large has been suggested as a source of apparent crystal lifetime increases at the highest dose rates (SI S9).

The present large and complete data set – spanning 26 crystals and more than 1300 intensity versus dose data sets — and the accompanying analysis establish that it is possible to outrun some damage at and near room temperature (but not at 100 K). At the largest nominal dose rate (~35 MGy/s), the half dose at and near 300 K is larger by a factor of roughly 1.5-2 than at typical crystallographic dose rates of ~10 kGy/s, for both thaumatin and lysozyme. In serial crystallography, this increase in crystal lifetime should translate into a comparable reduction in the number of required crystals and thus in data collection time per complete structural data set. Cooling to 260 K gives another factor of 1.5 increase in lifetime, and additional microfocusing to the 1 μm range (allowing a significant fraction of

photoelectrons to carry their energy out of the illuminated volume) could give an additional factor of ~2.

Together, the combination of intense microfocused synchrotron X-ray beams and modest reductions in data collection temperature below 300 K could allow a factor of 4-5 increase in data collection throughput. Even larger increases may be possible for crystals with larger room temperature radiation sensitivities (Warkentin *et al.*, 2014).

4. Conclusions

The evolution of diffracted intensities from protein crystals during irradiation by intense Gaussian X-ray microbeams is complex. Non-exponential integrated intensity decays, long interpreted in terms of sequential damage models, can arise from nonuniformity in crystal illumination, due to a nonuniform beam profile and/or due to sample rotation during illumination. Nonuniform illumination produces nonuniform damage, and for Gaussian beams to a surprising evolution of the diffraction-weighted crystal damage state with illumination time. Radiation-damage-induced reciprocal space peak broadening can lead to plateaus or initial increases of individual peak and integrated intensities with dose, mimicking the effect of a delayed onset of damage. These and other effects described here significantly complicate the extraction of reliable structure factors from measured intensities. This will be especially true when data is collected to near and beyond the half dose of the overall integrated intensity, and also to beyond the (smaller) half dose of the highest resolution shells; and when the dose per frame is a substantial fraction of the half dose, so that averaging over the non-monotonic evolution of individual peak intensities occurs and extrapolation to zero-dose intensity values is not possible. These conditions are likely to prevail in serial synchrotron crystallography using microfocused beams and microcrystals. Consequently, optimizing data collection protocols and maximizing the accuracy of extracted structure factors and structural models will require advances in modelling the complex spatiotemporal effects of radiation damage under these conditions.

Figure Captions

Figure 1 Representative semi-log plot of the integrated intensity in diffraction peaks versus dose at several dose rates, acquired from a single, fixed orientation lysozyme crystal at 300 K; Fig. SI-S5 shows 260 K data. Solid lines are single-parameter fits at the highest and lowest dose rates based on the model described here; dashed lines indicate the initial exponential trend. The intersection of the horizontal dashed black line with each dose curve determines the half dose $D_{1/2}$. Doses and dose rates in all figures are averages within the area of the Gaussian beam's FWHM.

Figure 2 (Top) Representative integrated intensity vs dose data for two thaumatin crystals at 260 K for a dose rate of 0.09 MGy/s. Each curve was recorded from one sample position. Sample 1 has an intensity variation with dose as in Fig. 1, while Sample 2 has an initial plateau in intensity. (Bottom) Sample 2's intensity plateau results from an initial growth with increasing dose of a subset of Bragg peaks that dominate the integrated intensity. Fig. SI-S6 shows similar data acquired at a dose rate of 36 MGy/s.

Figure 3 Half dose vs dose rate for tetragonal lysozyme at 100 K, 260 K, and 300 K. Similar plots are obtained for thaumatin, and half doses are summarized in Table S1. Each dose rate point represents an average of half doses determined from between 5 and 35 dose curves obtained from different positions on each sample. The different symbols at each temperature indicate data from different samples. The error bar on each point represents the corresponding standard deviation.

Figure 4 (Top) Diffracted flux from a crystal, proportional to the integrated intensity in Bragg peaks, versus dose, calculated for a Gaussian beam and for a beam with a top-hat (rectangular) profile of width equal to the Gaussian FWHM, for fixed crystal orientation during irradiation. The local decay of diffraction with dose is assumed to be exponential with a half dose $D_{1/2,\mathrm{local}}$ equal to that measured with a top-hat profile beam. (Bottom) Diffraction weighted dose DWD^* (40) and DWD (as revised here) versus normalized dose, for a Gaussian beam and fixed crystal.

Figure 5 (Top) Calculated diffracted flux per unit beam area and (bottom) per unit beam radius versus radius for equally spaced nominal doses, for a Gaussian beam and a locally exponential decay of diffraction with dose.

Acknowledgements We thank Giles Doumy for setting up the KB focusing mirrors, Anne Mulichak for growing some of the crystals used in these experiments, Clemens Schulz-Briese of Dectris, Inc., for a loan of the Pilatus3-300 K detector, and James Holton for pointing out the potential for detector undercounting when oscillation data are collected from low mosaicity crystals.

References

Ayyer, K., Philipp, H. T., Tate, M. W., Wierman, J. L., Elser, V. & Gruner, S. M. (2015). *IUCrJ*. **2**, 29–34.

Van Den Bedem, H., Dhanik, A., Latombe, J. C. & Deacon, A. M. (2009). *Acta Cryst. D*. **65**, 1107–1117.

Blake, C., Phillips, D., CCF, B. & DC, P. (1962). *Proc. Symp. Biol. Eff. Ioniz. Radiat. Mol. Lev.* 183–191.

Botha, S., Nass, K., Barends, T. R. M., Kabsch, W., Latz, B., Dworkowski, F., Foucar, L., Panepucci, E., Wang, M., Shoeman, R. L., Schlichting, I. & Doak, R. B. (2015). *Acta Cryst. D*. **71**, 387–397.

Coquelle, N., Brewster, A. S., Kapp, U., Shilova, A., Weinhausen, B., Burghammer, M. & Colletier, J. P. (2015). *Acta Cryst. D*. **71**, 1184–1196.

Coughlan, H. D., Darmanin, C., Kirkwood, H. J., Phillips, N. W., Hoxley, D., Clark, J. N., Harder, R., Maxey, E. & Abbey, B. (2016). *J. Synch. Rad.* 83–94.

Farley, C., Burks, G., Siegert, T. & Juers, D. H. (2014). *Acta Crystallogr. Sect. D Biol. Crystallogr.* **70**, 2111–2124.

Fenwick, R. B., van den Bedem, H., Fraser, J. S. & Wright, P. E. (2014). *Proc. Natl. Acad. Sci. U. S. A.* **111**, E445-54.

Finfrock, Y. Z., Stern, E. A., Alkire, R. W., Kas, J. J., Evans-Lutterodt, K., Stein, A., Duke, N., Lazarski, K. & Joachimiak, A. (2013). *Acta Cryst. D*. **69**, 1463–1469.

Fraser, J. S., Clarkson, M. W., Degnan, S. C., Erion, R., Kern, D. & Alber, T. (2009). *Nature*. **462**, 669–673.

Garman, E. F. (2010). *Acta Cryst. D*. **66**, 339–351.

Garman, E. F. & Owen, R. L. (2006). *Acta Crystallogr. Sect. D Biol. Crystallogr.* **62**, 32–47.

Gildea, R. J., Waterman, D. G., Parkhurst, J. M., Axford, D., Sutton, G., Stuart, D. I., Sauter, N. K., Evans, G. & Winter, G. (2014). *Acta Cryst. D*. **70**, 2652–2666.

Ginn, H. M., Roedig, P., Kuo, A., Evans, G., Sauter, N. K., Ernst, O., Meents, A., Mueller-Werkmeister, H., Miller, R. J. D. & Stuart, D. I. (2016). *Acta Cryst. D*. **72**, 956–965.

Hendrikson, W. (1976). *J. Mol. Biol.* **106**, 889–893.

Heymann, M., Opthalage, A., Wierman, J. L., Akella, S., Szebenyi, D. M. E., Gruner, S. M. & Fraden, S. (2014). *IUCrJ*. **1**, 349–360.

Holton, J. M. (2009). *J. Synch. Rad.* **16**, 133–142.

Holton, J. M., Classen, S., Frankel, K. A. & Tainer, J. A. (2014). *FEBS J.* **281**, 4046–4060.

Howells, M. R., Beetz, T., Chapman, H. N., Cui, C., Holton, J. M., Jacobsen, C. J., Kirz, J., Lima, E., Marchesini, S., Miao, H., Sayre, D., Shapiro, D. A., Spence, J. C. H. & Starodub, D. (2009). *J. Electron Spec. Rel. Phen.* **170**, 4–12.

Juers, D. H. & Matthews, B. W. (2004). *Q. Rev. Biophys.* **37**, 105–119.

Kabsch, W. (2010). *Acta Cryst. D*. **66**, 125–132.

Keedy, D. A., Kenner, L. R., Warkentin, M., Woldeyes, R. A., Hopkins, J. B., Thompson, M. C., Brewster, A. S., Benschoten, A. H. Van, Baxter, E. L., Uervirojnangkoorn, M., McPhilips, S. E., Song, J., Alonso-Mori, R., Holton, J. M., Weis, W. I., Brunger, A. T., Soltis, S. M., Lemke, H., Gonzalez, A., Sauter, N. K., Cohen, A. E., Van Den Bedem, H., Thorne, R. E. & Fraser, J. S. (2015). *Elife*. 7574.

Kriminski, S., Caylor, C. L., Nonato, M. C., Finkelstein, K. D. & Thorne, R. E. (2002). *Acta Cryst. D*. **58**, 459–471.

Lang, P. T., Ng, H.-L., Fraser, J. S., Corn, J. E., Echols, N., Sales, M., Holton, J. M. & Alber, T. (2010). *Protein Sci.* **19**, 1420–1431.

Leapman, R. D. & Sun, S. (1995). *Ultramicroscopy*. **59**, 71–79.

Leiros, H. S. H.-K. S. H.-K. S., Timmins, J., Ravelli, R. B. G. & McSweeney, S. M. (2006). *Acta Crystallogr. Sect. D Biol. Crystallogr.* **62**, 125–132.

Liebschner, D., Rosenbaum, G., Dauter, M. & Dauter, Z. (2015). *Acta Cryst. D*. **71**, 772–778.

Lyubimov, A. Y., Murray, T. D., Koehl, A., Araci, I. E., Uervirojnangkoorn, M., Zeldin, O. B., Cohen, A. E., Soltis, S. M., Baxter, E. L., Brewster, A. S., Sauter, N. K., Brunger, A. T. & Berger, J. M. (2015). *Acta Cryst. D*. **71**, 928–940.

Malkin, A. J. & Thorne, R. E. (2004). *Methods*. **34**, 273–299.

Meents, A., Gutmann, S., Wagner, A. & Schulze-Briese, C. (2010). *Proc. Natl. Acad. Sci.* **107**, 3–8.

Mueller, C., Marx, A., Epp, S. W., Zhong, Y., Kuo, A., Balo, A. R., Soman, J., Schotte, F., Lemke, H. T., Owen, R. L., Pai, E. F., Pearson, A. R., Olson, J. S., Anfinrud, P. A., Ernst, O. P. & Dwayne Miller, R. J. (2015). *Struct. Dyn.* **2**, 54302.

Nave, C. & Hill, M. A. (2005). *J. Synch. Rad.* **12**, 299–303.

Owen, R. L., Axford, D., Nettleship, J. E., Owens, R. J., Robinson, J. I., Morgan, A. W., Doré, A. S., Lebon, G., Tate, C. G., Fry, E. E., Ren, J., Stuart, D. I. & Evans, G. (2012). *Acta Cryst. D*. **68**,

810–818.

Owen, R. L., Paterson, N., Axford, D., Aishima, J., Schulze-Briese, C., Ren, J., Fry, E. E., Stuart, D. I. & Evans, G. (2014). *Acta Cryst. D*. **70**, 1248–1256.

Pflugrath, J. W. (2004). *Methods*. **34**, 415–423.

Rajendran, C., Dworkowski, F. S. N., Wang, M. & Schulze-Briese, C. (2011). *J. Synchrotron Radiat.* **18**, 318–328.

Ravelli, R. B. G. & McSweeney, S. M. (2000). *Structure*. **8**, 315–328.

Ravelli, R. B. G., Theveneau, P., Mcsweeney, S. & Caffrey, M. (2002). *J Synch Rad*. **9**, 355–360.

Roessler, C. G., Kuczewski, A., Stearns, R., Ellson, R., Olechno, J., Orville, A. M., Allaire, M., Soares, A. S. & Heroux, A. (2013). *J. Synch. Rad.* **20**, 805–808.

Sanishvili, R., Yoder, D. W., Pothineni, S. B., Rosenbaum, G., Xu, S., Vogt, S., Stepanov, S., Makarov, O. A., Corcoran, S., Benn, R., Nagarajan, V., Smith, J. L. & Fischetti, R. F. (2011). *Proc. Natl. Acad. Sci. U. S. A.* **108**, 6127–6132.

Sauter, N. K. (2010). *Comput. Crystallogr. Newsl.* **1**, 18–23.

Shimizu, N., Hirata, K., Hasegawa, K., Ueno, G. & Yamamoto, M. (2007). *J. Synchrotron Radiat.* **14**, 4–10.

Sliz, P., Harrison, S. C. & Rosenbaum, G. (2003). *Structure*. **11**, 13–19.

Smith, J. L., Fischetti, R. F. & Yamamoto, M. (2012). *Curr. Opin. Struct. Biol.* **22**, 602–612.

Southworth-Davies, R. J., Medina, M. A., Carmichael, I. & Garman, E. F. (2007). *Structure*. **15**, 1531–1541.

Stellato, F., Oberth??r, D., Liang, M., Bean, R., Gati, C., Yefanov, O., Barty, A., Burkhardt, A., Fischer, P., Galli, L., Kirian, R. A., Meyer, J., Panneerselvam, S., Yoon, C. H., Chervinskii, F., Speller, E., White, T. A., Betzel, C., Meents, A. & Chapman, H. N. (2014). *IUCrJ*. **1**, 204–212.

Sygusch, J. & Allaire, M. (1988). *Acta Cryst.* **A44**, 443–448.

Warkentin, M., Badeau, R., Hopkins, J. B., Mulichak, A. M., Keefe, L. J. & Thorne, R. E. (2012). *Acta Crystallogr. Sect. D Biol. Crystallogr.* **68**, 124–133.

Warkentin, M., Hopkins, J. B., Badeau, R., Mulichak, A. M., Keefe, L. J. & Thorne, R. E. (2013). *J. Synch. Rad.* **20**, 7–13.

Warkentin, M., Hopkins, J. B., Haber, J. B., Blaha, G. & Thorne, R. E. (2014). *Acta Cryst. D*. **70**, 2890–2896.

Warkentin, M. & Thorne, R. E. (2010*a*). *Acta Cryst. D*. **66**, 1092–1100.

Warkentin, M. & Thorne, R. E. (2010*b*). *J. Struct. Funct. Genomics*. **11**, 85–89.

White, T. A., Mariani, V., Brehm, W., Yefanov, O., Barty, A., Beyerlein, K. R., Chervinskii, F., Galli, L., Gati, C., Nakane, T., Tolstikova, A., Yamashita, K., Yoon, C. H., Diederichs, K. & Chapman, H. N. (2016). *J. Appl. Cryst.* **49**, 680–689.

Zeldin, O. B., Brockhauser, S., Bremridge, J., Holton, J. M. & Garman, E. F. (2013). *Proc. Natl. Acad. Sci. U. S. A.* **110**, 20551–20556.

Zeldin, O. B., Gerstel, M. & Garman, E. F. (2013). *J. Appl. Crystallogr.* **46**, 1225–1230.

Zhang, Z., Sauter, N. K., Van Den Bedem, H., Snell, G. & Deacon, A. M. (2006). *J. Appl. Crystallogr.* **39**, 112–119.

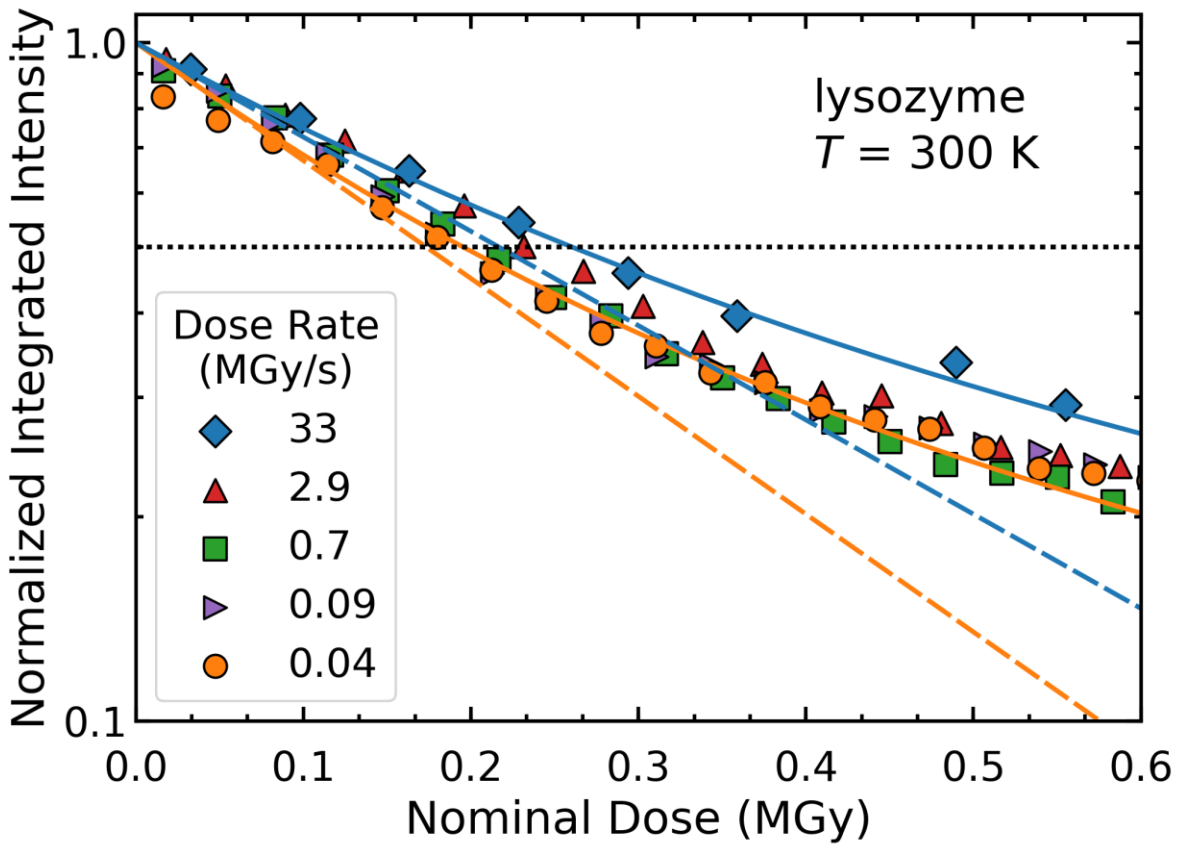
lysozyme
T = 300 K
Dose Rate
(MGy/s)
33
2.9
0.7
0.09
0.04
Normalized Integrated Intensity
1.0
0.1
0.0
0.1
0.2
0.3
0.4
0.5
0.6
Nominal Dose (MGy)

Figure 1

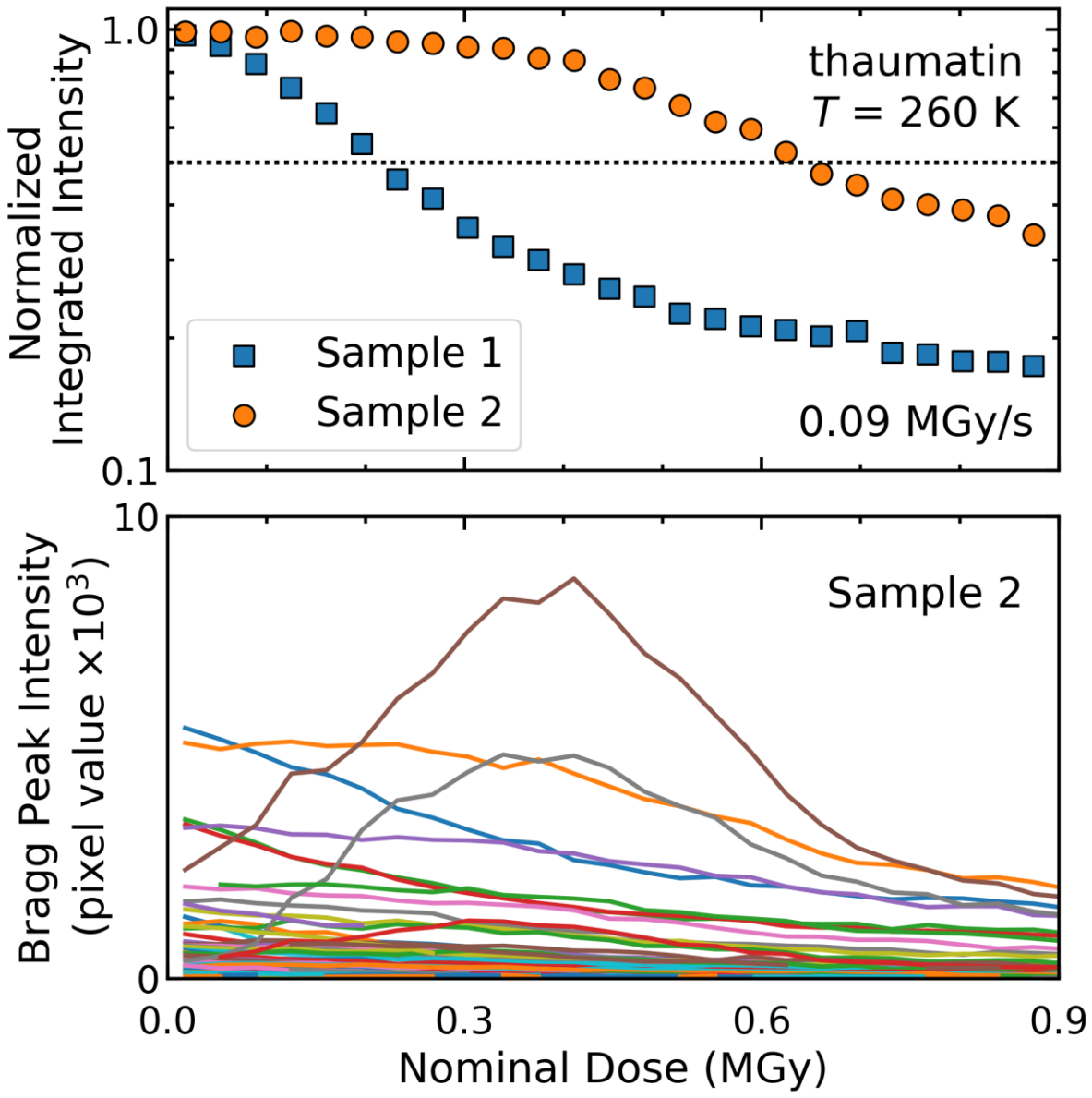
Normalized Integrated Intensity
1.0
0.1
thaumatin
T = 260 K
Sample 1
Sample 2
0.09 MGy/s
Bragg Peak Intensity (pixel value ×10³)
10
0
Sample 2
0.0
0.3
0.6
0.9
Nominal Dose (MGy)

Figure 2

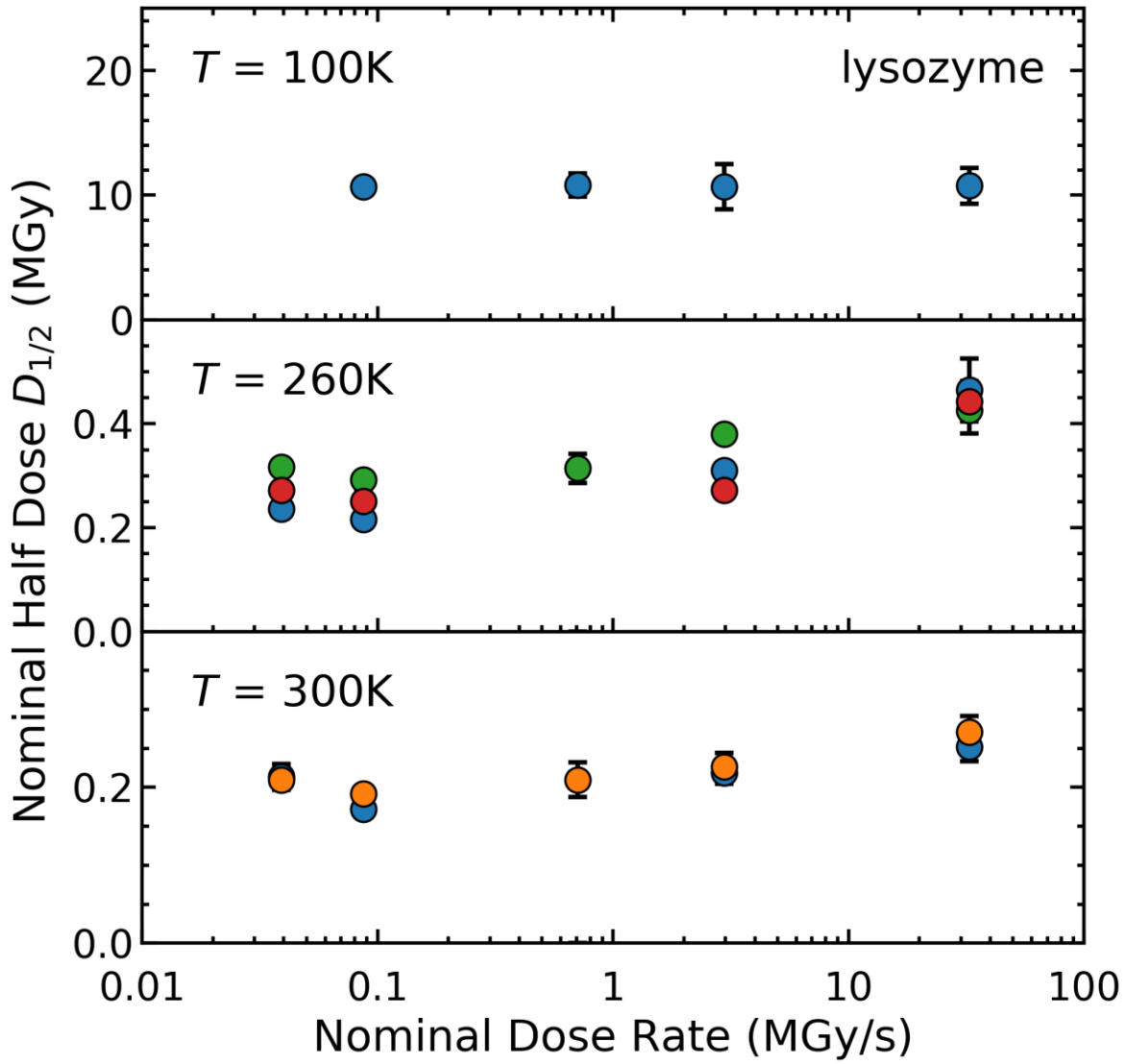
T = 100K
lysozyme
T = 260K
T = 300K
Nominal Half Dose $D_{1/2}$ (MGy)
Nominal Dose Rate (MGy/s)
0.01
0.1
1
10
100
0
10
20
0.0
0.2
0.4
0.0
0.2

Figure 3

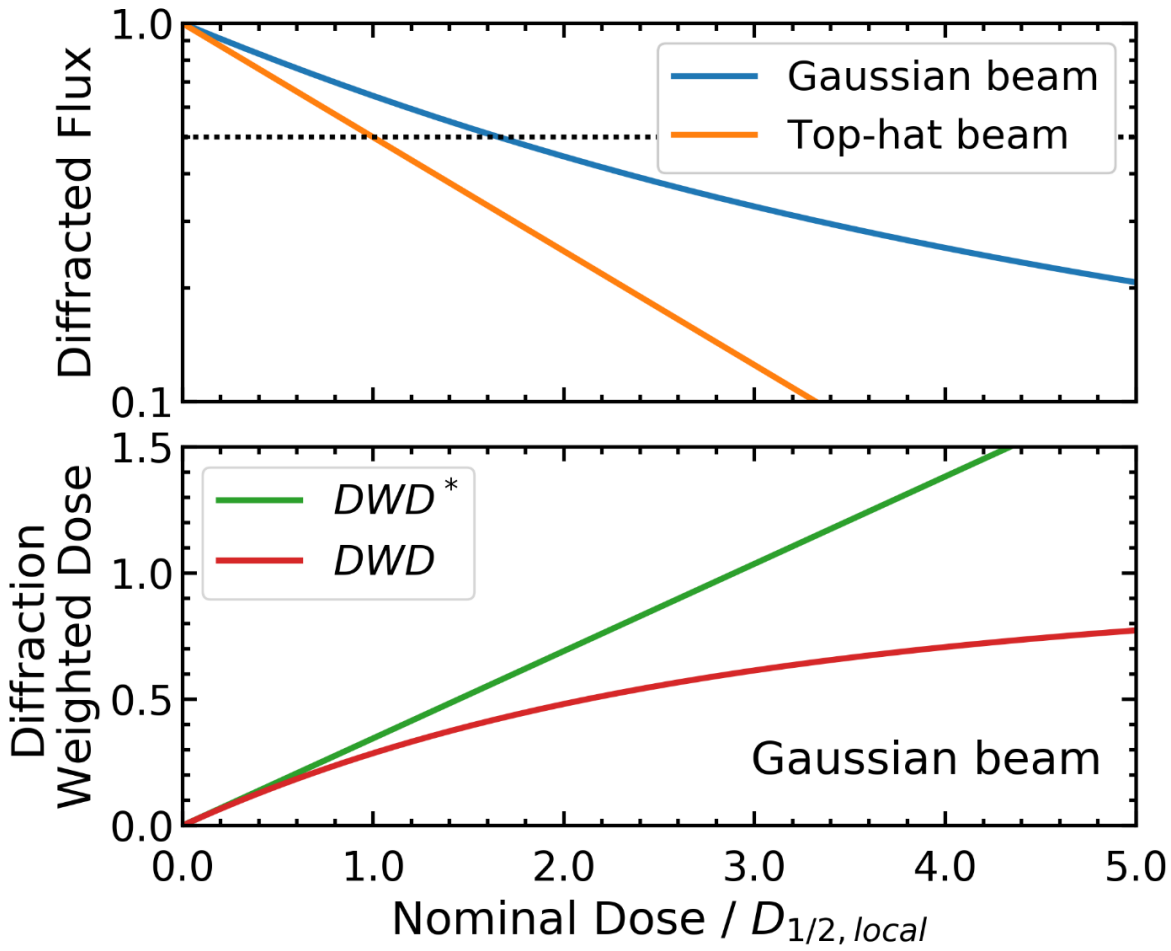
1.0
0.1
Diffracted Flux
Gaussian beam
Top-hat beam
1.5
1.0
0.5
0.0
Diffraction Weighted Dose
DWD*
DWD
Gaussian beam
0.0
1.0
2.0
3.0
4.0
5.0
Nominal Dose / D1/2, local

Figure 4

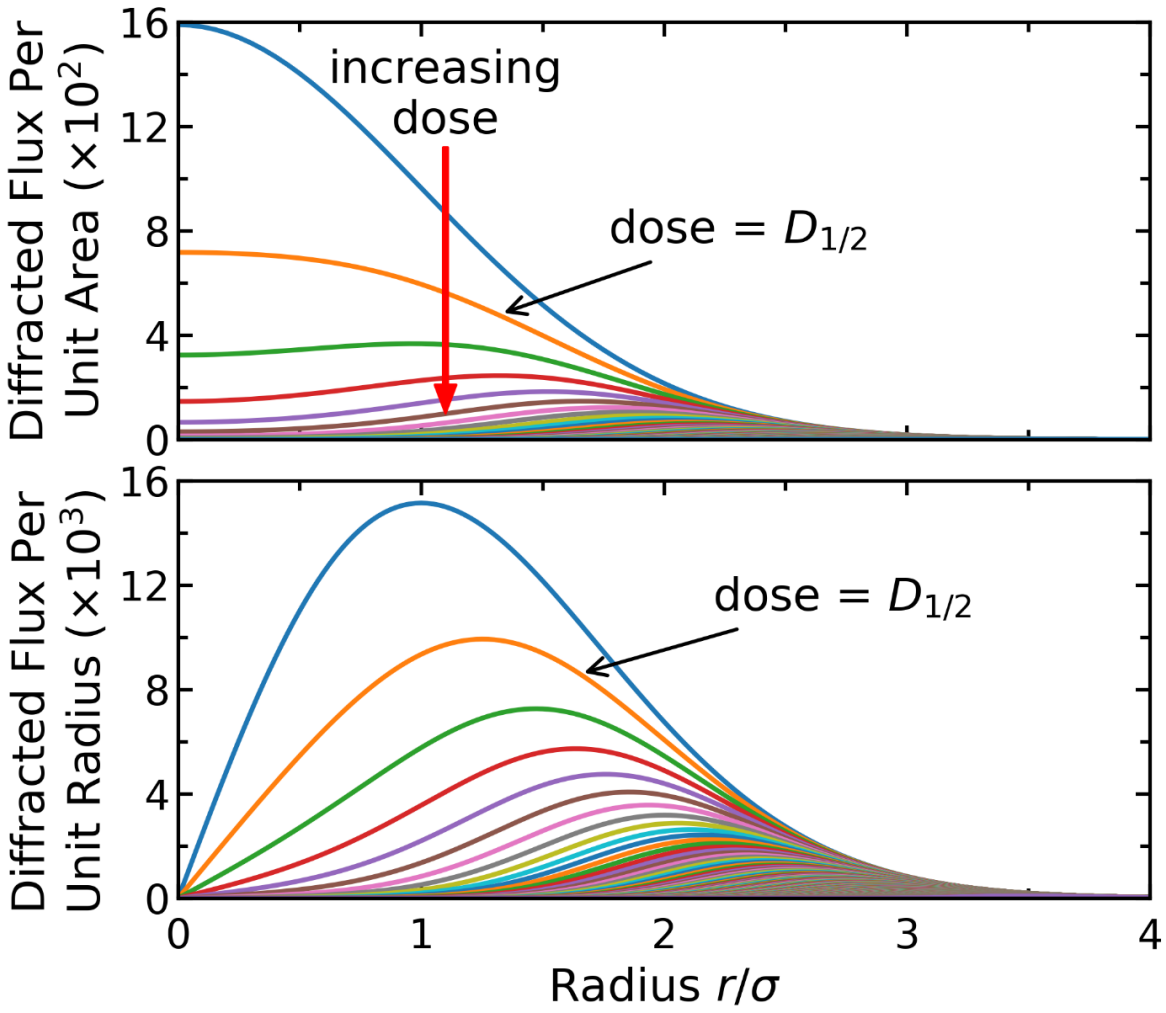
Diffracted Flux Per Unit Area (×10²)
increasing dose
dose = $D_{1/2}$
Diffracted Flux Per Unit Radius (×10³)
dose = $D_{1/2}$
Radius r/σ
0
4
8
12
16
0
1
2
3
4

Figure 5

Supporting information

S1. Crystallization method and conditions

Tetragonal thaumatin and tetragonal lysozyme crystals were grown in 24-well plates using the hanging-drop vapour diffusion method. Purified powders of thaumatin and lysozyme (3× recrystallized) were purchased from Sigma-Aldrich (St Louis, Missouri, USA). Thaumatin was dissolved to a concentration of 25 mg ml^{-1} in 100 m*M* potassium phosphate buffer at pH 6.8, and a well s

olution prepared by adding 1 *M* sodium potassium tartrate to the same buffer. Lysozyme was dissolved in 0.5 M sodium chloride and a well solution containing 1 M sodium chloride prepared. 10 µl drops obtained by mixing 5 µl each of protein and well solution were suspended over 500 µl of well solution.

S2. Crystal handling and data collection times

The time between crystal mounting in oil on a loop and data collection was typically 5 minutes, and the time required for collection of all data sets from each crystal was typically 15-30 minutes. The oil alone, without any capillary enclosure, was sufficient to prevent crystal dehydration during this period, as was verified by monitoring unit cell parameters and by collecting data with oil-coated crystals contained in polymer capillaries.

S3. Spatial spread of radiation damage

Diffraction data was collected from a series of positions on each sample, separated by 20 µm. As a test, a sample at 300 K was irradiated one position with a large dose (several times the half-dose), and then diffraction measurements were acquired using a low dose in 10 and 20 µm steps along perpendicular lines meeting at that dosed position. These measurements confirmed that damage from each irradiated position did not extend to adjacent positions. All effects reported – including intensity fluctuations with dose at the highest dose rates and integrated intensity plateaus – were equally likely to be observed in newly irradiated crystal regions as when previously irradiated spots were nearby. As discussed in S5 below, the broadening of the damage footprint due to photoelectron escape at the X-ray energy used is small compared with the beam size. Free radical mean free paths at room temperature in the high protein density environment of a crystal should be less than 1 µm. More likely causes of damage spreading are inhomogeneous stresses associated with the internal pressure increase caused by generation of defects and hydrogen, and plastic lattice failure and cracking at larger doses. However, the irradiated spot area of ~ 3 µm × 5 µm ~ 15 μm^2 is small compared with the 20 µm × 20 µm ~ 400 μm^2 allocated to each measurement, and so the amount of "spread" damage in any adjacent spot will be tiny compared with damage due to direct irradiation of that spot.

S4. Visual manifestations of X-ray beam – crystal interactions

Microbeam irradiation had two visual consequences. First, the irradiated positions of each crystal became visible as an array of cylinders (Fig. S3), due to small (~10^{-4}) fractional changes in refractive index associated with radiation-induced changes in unit cell volume and density. Second, at the highest dose rates optical fluorescence from the region being irradiated was clearly visible using the beamline telescope and camera (Fig. S4), especially at T=100 K where the decay time of the fluorescence following irradiation was several seconds. The power (intensity) associated with this fluorescence was a small fraction of the ~2 mW (1.2×10^8 W/m^2) of the incident X-rays.

S5. Effect of photoelectron escape on dose estimates

For sufficiently small microfocused volumes (or sufficiently small crystals), X-ray generated photoelectrons and fluorescent photons may leave the illuminated volume and deposit their energy outside of it, reducing the dose received, with the photoelectrons carrying most of the energy. Measurements using 18.5 keV microfocused Gaussian profile beams found that for 2.7 μm FWHM and 5.35 μm beams, the integrated intensity loss per unit dose was ~0.65 and 0.8, respectively, of that obtained using a 15.6 μm beam . For the 10 keV X-rays used here, photoelectron ranges should be smaller by a factor of roughly 3 (Stern *et al.*, 2009; Finfrock *et al.*, 2013, 2010). The reduction in actual dose due to photoelectron escape within our 2.4 × 5.1 FWHM beams should be less than 10%. Note that this effect is independent of dose rate and only weakly temperature dependent, and so will not affect radiation sensitivity ratios at different dose rates and temperatures.

S6. Effect of diffraction peak integration parameter choices on half-dose estimates

Diffraction peak intensities depend on parameters used to model and integrate the peak and background. These choices also affect how individual and frame-integrated peak intensities vary with dose, and the calculated half-dose values at which the integrated diffraction intensity decreases to half its initial value. However, for comparably exposed frames – acquired at different dose rates, from different samples, or at different temperatures – the ratio of half-doses is relatively insensitive to these choices. As a check on effects of frame integration parameters, integrated intensities versus dose were calculated by integrating only the 10, 25, and 50 brightest peaks in each frame, and compared with results for integration of all peaks. Except for very weakly exposed frames acquired, e.g., at the edge of a crystal, or when a few very bright peaks behaved differently (e.g., showed a large initial intensity rise) than most other peaks, the intensity versus dose curves and half dose values from these different integrations were consistent.

S7. Effect of Gaussian beam anisotropy

Although the model presented here assumes a circularly symmetric 2D Gaussian beam, the quantitative predictions are the same for anisotropic beams of the form

$$F(r,t) = F_0 \frac{1}{2\pi\sigma_x\sigma_y} e^{-\left(\frac{x^2}{2\sigma_x^2}+\frac{y^2}{2\sigma_y^2}\right)},$$

and so apply to the reported data collected with a 2.4 × 5.1 μm beam.

S8. Previous experiments on the time and dose rate dependence of radiation damage

The dose rate and thus time dependence of damage, relevant to high flux density microcrystallography, has been controversial. Initial experiments at dose rates up to 10 kGy/s in most cases found no dose rate dependence. Observations of dark progression — an increase in damage while the X-ray beam is turned off — versus temperature between 180 K and 240 K revealed a temperature-activated component of damage whose time scale extrapolated to ~1 s at 300 K, suggesting that X-ray data collection on shorter timescales could allow some fraction of radiation damage to be outrun (Warkentin *et al.*, 2011). Experiments using ~50 μm beams found that dose rates of ~680 kGy/s gave damage-limited crystal lifetimes for thaumatin crystals at 260 K ~50% larger than at typical crystallographic dose rates of ~10 kGy/s (Warkentin *et al.*, 2012), and that dose rates approaching ~1 MGy/s increased 300 K lifetimes of three crystal systems by 30-80% (Owen *et al.*, 2012).

Using 10 and 20 μm microfocused beams and the same Pilatus3-300 K detector (i.e, the identical unit, not just the same model, loaned by Dectris) used in the present experiments, integrated intensity versus dose data was observed to exhibit an initial plateau or region of reduced slope, which was described as a "lag phase," for dose rates above 1 MGy (Owen *et al.*, 2014). Measuring crystal lifetime using D_{85}, the dose at which the integrated diffraction intensity is reduced to 85% of its initial value, thaumatin crystal lifetimes at 300 K measured using a dose rate of 1.32 MGy/s were found to be almost a factor of four larger than with a dose rate of 0.36 MGy/s. Combining data for bovine enterovirus serotype 2 (BEV2) from two experiments using different detectors, D_{85} at 5 MGy/s was found to be roughly 7 times larger than at dose rates below 500 kGy/s. These large increases in apparent crystal lifetime were due to initial intensity plateaus (the "lag phase"), and because initial intensity plateaus have a larger effect on D_{85} than on $D_{1/2}$. By examining individual diffraction peak intensities versus dose, the plateaus and "lag phase" are shown here to be an artefact of how diffraction data was collected. The plateaus and D_{85} values calculated when they are present do not indicate an initially reduced rate of radiation damage.

S9. Effects of detector saturation on measured intensities

At high incident (on the detector area) photon flux densities, single photon counting detectors undercount due to incoming pulse pile-up. Each pixel in the array has a finite dead time or retrigger time following detection of a photon before it can detect another photon, and this leads to increased undercounting as the incident flux increases. Provided that scattering from the sample itself does not change during each frame, the statistics of photon arrival, including effects of synchrotron bunch structure, can be modeled and a dead time correction applied to the "raw" detected counts to extend the detector's effective linear response range to higher count rates. The Pilatus3-300 K detector used here has a maximum usable incoming photon count rate per pixel in excess of 10 Mcps, with a dead-time corrected error at 10 Mcps of less than 10%.

The maximum measured count rate per pixel observed in the ~50,000 frames of the present experiments, obtained when using the unattenuated beam, was ~ 11 Mcps. To investigate possible errors introduced at large count rates, every pixel with count rates larger than 5 Mcps was flagged, and a histogram of these high count rate pixels generated for the first frame of every dose series (in which pixel count rates were usually largest). These histograms then allowed the integrated intensity and individual peak intensities versus dose curves to be compared based on first frame pixel count rates.

No effects whatsoever of maximum pixel count rates and number of high count rate pixels on the integrated or individual peak intensity versus dose curves were found. Between 16 and 50 dose curves were collected using the unattenuated beam from each crystal, each with the same crystal orientation but at a different position on the crystal. Due to variations in crystal thickness with position, some positions yielded first frames with up to 14 pixels having count rates >5 Mcps, while other positions had no high count rate pixels. These crystal positions all yielded quantitatively similar dose curves, half-doses, and individual peak intensity vs frame curves. There was also no correlation between maximum count rates per frame and the presence of plateaus in the dose curves. 39 of the 212 dose curves acquired from thaumatin crystals at the maximum dose and count rates showed initial plateaus or significantly reduced slopes, and none of the 271 dose curves acquired from lysozyme at the maximum dose rate showed plateaus. Plateaus were observed for all dose rates (attenuator settings), and at the lowest dose rate pixel count rates were ~10 kcps or smaller.

Pulse pile-up / dead time corrections can fail if the statistics of photon arrival during an exposure does not match model assumptions. This can happen during oscillations using very small mosaicity crystals, where a very bright peak may "flash" on and off in a time short compared with the pixel exposure time. Since the dead time correction is applied to the total recorded counts, it may under-correct counts recorded during the flash. In a dose series where the intensities of peaks decay from

frame to frame, undercounting due to such count correction errors will be largest in the initial, brightest frames, and so may cause an initial flattening of the dose curve.

Even though all the data collected here was from crystals in fixed orientations, sample position and orientation changes could in principle have occurred due to vibration in the gas stream (at 100 K and 260 K), and due to crystal sedimentation (at 260 K and especially 300 K). At 100 K, crystal mosaicities are large (~0.3° or more) and so count rates should be relatively immune to motions. At all temperatures, count rate corrections and undercounting could only have been an issue when using the unattenuated beam, for which the detector measurement time per frame was 1 ms. Only very large and/or high frequency motions could produce mosaic-width-size orientation changes on this timescale. To check for sample motions, intensity versus frame number plots for the diffraction peaks in all 1300 dose series were manually inspected. Since detector frame rates varied from 500 Hz to 1.2 Hz, these data were sensitive to motions on a wide range of time scales. In a few dose series, the amplitudes of individual peaks were observed to fluctuate with frame number, suggesting sample motion, but this was the rare exception, and these frames were excluded from our analysis.

S10. Origin of integrated intensity plateaus and site-specific radiation damage

Variations in relative diffraction peak intensities with dose, the cause of plateaus in integrated intensity observed here, can also arise from site-specific damage, i.e., from radiation-induced atomic displacements that are correlated between unit cells (e.g., breaking of disulphide bonds, reduction of metal centers) that result in changes in the underlying structure factors (Wei *et al.*, 2000). For fixed crystal orientation and fixed dose rate, bond breaking and other site-specific damage and thus the evolution of peak intensities with dose should be independent of crystal position, since the microscopic details of molecular damage should depend only on dose and crystal composition.

In fact, the rise and fall of individual Bragg peak intensities observed here is strongly position dependent, presumably because the evolution of mosaicity and/or lattice strain with dose at each position depends on local crystal thickness, proximity to crystal facets or edges, and the details of irradiation-induced fracturing and plastic failure within each illuminated volume.

The integrated intensity plateaus observed here and in Ref. (Owen *et al.*, 2014) were recorded using a Pilatus3-300 K detector, which was positioned with its lower edge just above the beam and recorded roughly 1/3 of the full diffraction pattern. Recording full frames (using, e.g., a Pilatus 6M detector) should modestly reduce but not eliminate the plateaus and the orientation-dependent variations in integrated intensity versus dose.

S11. Estimates of X-ray beam heating

In the present experiments, X-ray beam microfocusing increased the flux density and dose rate by a factor of ~10^3 relative to the X-ray beam exiting the monochromator, a gave a peak

X-ray intensity at the sample of ~0.2 mW/μm^2. We previously showed that, provided the beam is small compared with the crystal size, microfocusing produces only modest increases in temperature within the illuminated volume. For a cylindrical X-ray beam and cylindrical sample, the maximum steady-state temperature rise in the illuminated volume is (Warkentin *et al.*, 2012)

$$\Delta T(r_1) = \frac{D'\rho r_1^2}{2k}\left[\log\left(\frac{r_2}{r_1}\right) + \frac{k}{hr_2}\right]$$

Here D' is the dose rate, ρ is the sample density, k is the sample thermal conductivity, h is the heat transfer coefficient at the sample surface, r_1 is the beam radius, and r_2 is the sample radius. Using D' = 30 MGy/s, ρ = 1200 kg/m^3, k = 0.6 W/mK (the value for water at 300 K), h=290 W/m^2/K at 300 K (Kriminski *et al.*, 2003), r_1 = 2 μm, and r_2 = 50 μm gives $\Delta T \approx 6$ K. This is small compared to the temperature change required to appreciably affect the rate of radiation damage at all temperatures studied.

Note also that heating raises the crystal temperature, and that radiation damage per unit dose increases with temperature. Consequently, X-ray beam heating at the highest dose rates used here should make crystals appear more radiation sensitive; in fact, they are found to be less radiation sensitive than at lower dose rates.

Sample heating will be much larger if the beam and crystal sizes are comparable. For an upper bound estimate, assume a crystal size equal to the FWHM and that heating is adiabatic. With a dose rate of 30 MGy/s within the FWHM, this gives an initial heating rate of ~ 7 K/ms and a temperature rise during irradiation to the half-dose at T=300 K of ~100 K. For a beam size equal to the sample size (r_1=r_2), the above equation for a long cylindrical sample gives a steady state temperature rise of ~125 K; for a sample of length (along the beam) comparable to its diameter, heat transfer will be more effective than in the long-cylinder approximation leading to the above expression and the steady state temperature rise will be smaller.

S12. Origin of non-exponential decays of integrated intensities

Non-exponential decays of integrated intensities with dose or irradiation time, with more gradual decays observed at large doses/irradiation times, have been frequently observed in previous experiments using protein crystals, including those using X-ray microbeams. The non-exponential behavior has been analysed using models that consider local dose-dependent transitions between undamaged protein, partially disordered protein, and fully amorphous protein, which give rise to a locally non-exponential variation of diffracted intensity with dose. However, Gaussian X-ray beams – and, more generally, any spatially non-uniform X-ray dosing of the crystal – will give nonexponential decays of the diffracted intensity even if the underlying local relationship between diffracted intensity and dose is purely

exponential. This is true even if the X-ray beam has a "top-hat" profile, and nonuniform irradiation is due to, e.g, crystal rotation or displacement.

For example, suppose a crystal is illuminated with a square, uniform profile beam and that the crystal is translated in a series of steps that are small compared with the beam size during irradiation. On first turning on the beam the intensity will decay exponentially with dose delivered to the crystal. But as the crystal is translated, the unexposed region that moves into the beam in each step will contribute more to the total diffracted intensity than previously exposed and damaged regions that remain in the beam. For doses per step interval that are comparable to the local half-dose, after a few steps essentially all the diffraction will come from newly illuminated crystal, the diffracted intensity (averaged over the time for one step) will become independent of dose delivered to the crystal and time, and the diffraction weighted dose DWD will become independent of dose and time. As a second example, suppose that a large crystal is illuminated by a smaller top-hat beam, that the crystal is repeatedly rotated through the same small (say, 5°) angular wedge during data collection, and that the integrated diffraction intensity collected during each rotation plotted versus time or total dose. As the dose in the central, continuously illuminated region of the wedge increases through the half-dose, more and more of the diffracted intensity from each wedge will come from the relatively undamaged crystal regions that are only transiently illuminated at the extreme limits of the rotation. The integrated intensity will then deviate upward from the exponential decay describing the local damage response. This wedge data collection mode was used in previous radiation damage studies by some of the present authors, where non-exponential decays were analysed using the local damage models.

Additional deviation from exponential decays at large doses will arise because there is no single half dose $D_{1/2,\mathrm{local}}$ or exponential decay constant D_{e} value that can describe the decay of Bragg peak intensities at all angles and resolutions. Low resolution Bragg peaks correspond to long wavelength Fourier components of the electron density, and much more dose and damage are needed to disrupt crystal structure and electron density on large length scales than on short length scales. This is discussed and experimentally demonstrated over three orders of magnitude in resolution by Howells et al. (Howells *et al.*, 2009). Note that this behavior is in some sense fundamental to radiation damage, and does not require invocation of a three-state model or any other particular model for the microscopic nature of damage.

S13. Implications for structure factor determination in the presence of radiation damage

As will be discussed in more detail elsewhere, the present results are of particular importance when data is collected to "large" doses, and/or when data collection involves substantial doses per frame. "Large" means comparable to the half-dose, which depends on the initial diffraction resolution of the crystal; crystals that initially diffract to high resolution have smaller half-doses and so are more likely to receive "large" doses. For data collection to large doses (e.g., during a rotation series), the complex spatiotemporal evolution of diffraction within the illuminated volume and the distribution of damage

states within that volume will make it difficult to extract true structure factors from the measured Bragg peak intensities without modelling. In serial crystallography using high flux microfocused beams and microcrystals, crystals may receive large doses in a single recorded frame, and the measured Bragg peak intensities will average over the complex spatio-temporal evolution of diffraction during that frame. Note also that models currently used to extrapolate measured structure factors to their zero-dose values do not account for the effects described here, and may lead to large errors when, e.g., the exposure per frame is not small.

S14. Comparison of diffraction intensities and half doses generated using DISTL and XDS

Both XDS and DISTL were used to identify and integrate individual diffraction peaks in our diffraction frames, which consisted of time/dose series with the crystal held in a fixed orientation. The intensities of those peaks were then summed to generate integrated intensity (across the frame) versus dose plots. With our parameter optimization efforts, XDS provided more accurate and consistent peak identification in our still frames. DISTL was more likely to identify spurious peaks, and was more likely to fail in processing individual frames in a dose series. However, background-subtracted peak intensities reported by XDS are I/σ values (W. Kabsch, private communication), not absolute intensities as in DISTL, and so integrating the XDS output for each frame added a background and thus resolution-dependent weighting to the intensities.

Despite this weighting of individual peak intensities, the XDS-derived integrated frame intensities and their dose and dose rate dependence had all the same qualitative features as were observed using DISTL results, including initial plateaus in integrated intensities and larger half-doses at the highest dose rates. Half doses calculated using XDS agreed to within 15% of those determined using DISTL. Figure S10 shows XDS results for integrated intensity versus dose for lysozyme at T=260 K, corresponding to the DISTL results shown in Fig. S5. Figure S11 shows XDS results for integrated intensity and individual peak intensities corresponding to the results in Fig. S6.

SI References

Finfrock, Y. Z., Stern, E. A., Alkire, R. W., Kas, J. J., Evans-Lutterodt, K., Stein, A., Duke, N., Lazarski, K. & Joachimiak, A. (2013). *Acta Cryst. D*. **69**, 1463–1469.

Finfrock, Y. Z., Stern, E. A., Yacoby, Y., Alkire, R. W., Evans-Lutterodt, K., Stein, A., Isakovic, A. F., Kas, J. J. & Joachimiak, A. (2010). *Acta Crystallogr. Sect. D*. **66**, 1287–1294.

Howells, M. R., Beetz, T., Chapman, H. N., Cui, C., Holton, J. M., Jacobsen, C. J., Kirz, J., Lima, E., Marchesini, S., Miao, H., Sayre, D., Shapiro, D. A., Spence, J. C. H. & Starodub, D. (2009). *J.*

Electron Spec. Rel. Phen. **170**, 4–12.

Kriminski, S., Kazmierczak, M. & Thorne, R. E. (2003). *Acta Cryst. D*. **59**, 697–708.

Owen, R. L., Axford, D., Nettleship, J. E., Owens, R. J., Robinson, J. I., Morgan, A. W., Doré, A. S., Lebon, G., Tate, C. G., Fry, E. E., Ren, J., Stuart, D. I. & Evans, G. (2012). *Acta Cryst. D*. **68**, 810–818.

Owen, R. L., Paterson, N., Axford, D., Aishima, J., Schulze-Briese, C., Ren, J., Fry, E. E., Stuart, D. I. & Evans, G. (2014). *Acta Cryst. D*. **70**, 1248–1256.

Sanishvili, R., Yoder, D. W., Pothineni, S. B., Rosenbaum, G., Xu, S., Vogt, S., Stepanov, S., Makarov, O. A., Corcoran, S., Benn, R., Nagarajan, V., Smith, J. L. & Fischetti, R. F. (2011). *Proc. Natl. Acad. Sci. U. S. A.* **108**, 6127–6132.

Stern, E. a, Yacoby, Y., Seidler, G. T., Nagle, K. P., Prange, M. P., Sorini, A. P., Rehr, J. J. & Joachimiak, A. (2009). *Acta Crystallogr. D. Biol. Crystallogr.* **65**, 366–374.

Warkentin, M., Badeau, R., Hopkins, J. B., Mulichak, A. M., Keefe, L. J. & Thorne, R. E. (2012). *Acta Crystallogr. Sect. D Biol. Crystallogr.* **68**, 124–133.

Warkentin, M., Badeau, R., Hopkins, J. & Thorne, R. E. (2011). *Acta Crystallogr. Sect. D Biol. Crystallogr.* **67**, 792–803.

Wei, K, M., Ravelli, R. B. G., Kryger, G., McSweeney, S., Raves, M. L., Harel, M., Gros, P., Silman, I., Kroon, J. & Sussman, J. L. (2000). *PNAS*. **97**, 623–628.

Table S1 Half doses versus dose rate at 100 K, 260 K, and 300 K for tetragonal lysozyme and thaumatin crystals. Each half dose value is an average of values obtained from between 5 and 35 positions on each crystal and, at 260 and 300 K, multiple crystals. The uncertainties represent the standard deviations of all measured values at each temperature.

	Dose Rate (MGy/s)	**Half Dose $D_{1/2}$ (MGy) T=100 K**	**Half Dose $D_{1/2}$ (MGy) T=260 K**	**Half Dose $D_{1/2}$ (MGy) T=300 K**
lysozyme	0.039	-	0.27 ± 0.01	0.21 ± 0.02
	0.087	10.7 ± 0.5	0.25 ± 0.02	0.18 ± 0.01
	0.71	10.8 ± 0.9	-	0.21 ± 0.02
	2.97	10.7 ± 1.8	0.32 ± 0.02	0.22 ± 0.02
	32.6	10.8 ± 1.4	0.44 ± 0.08	0.26 ± 0.03
thaumatin	0.042	13.8 ± 0.5	0.41 ± 0.02	-
	0.095	12.6 ± 0.2	0.39 ± 0.04	0.16 ± 0.04
	0.77	-	-	0.20 ± 0.05
	3.24	14.5 ± 0.6	0.43 ± 0.04	0.22 ± 0.02
	35.6	12.3 ± 0.9	0.49 ± 0.05	0.35 ± 0.01

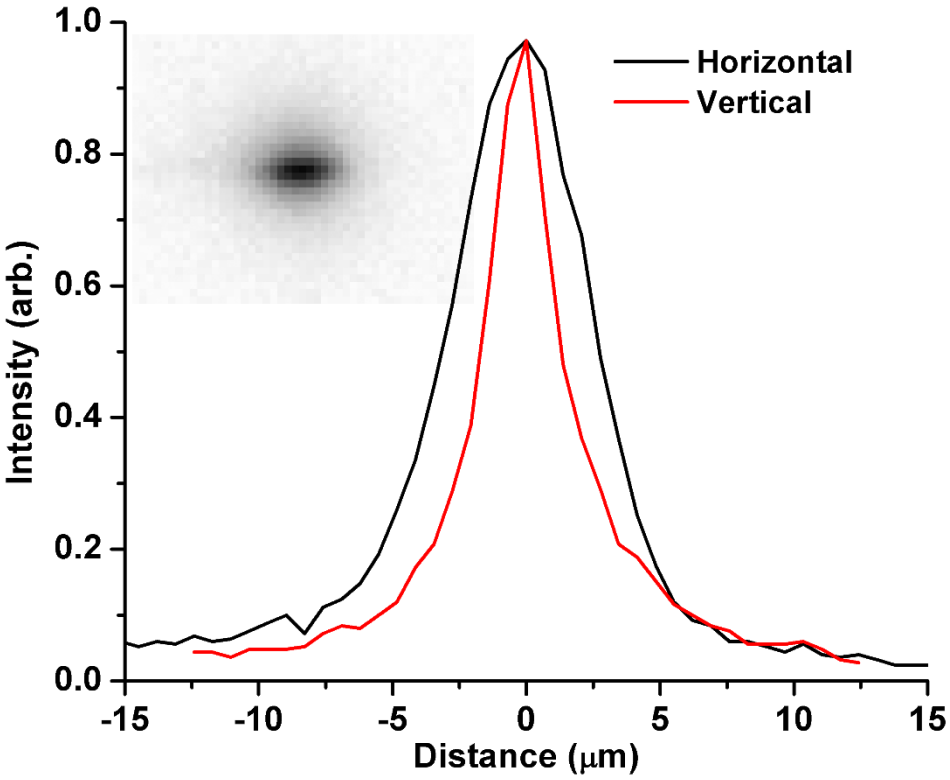

Figure S1 Microfocused X-ray beam profile determined by scanning a GaAs wafer edge through the beam and recording the detected intensity. The inset shows an image of the attenuated beam.

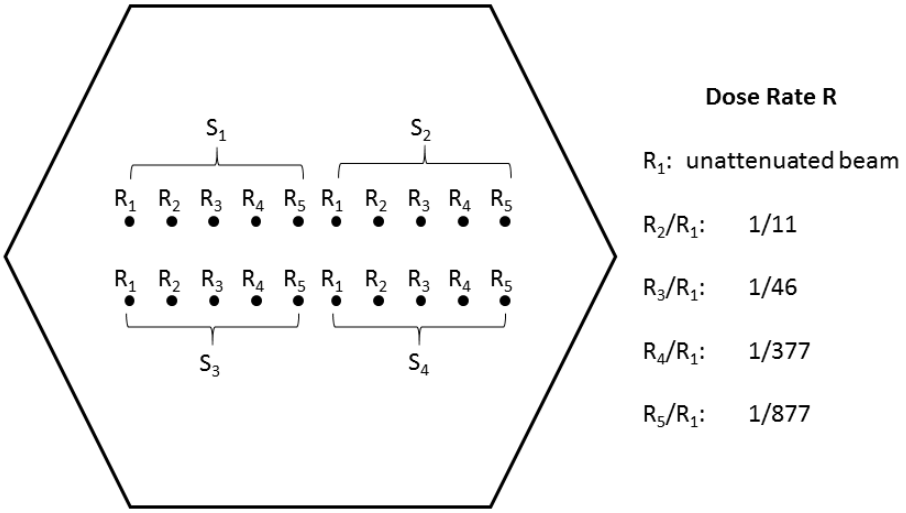

Figure S2 Example crystal irradiation pattern. Solid black dots represent irradiated positions. Each dose rate series S involved irradiating the crystal at 5 consecutive positions (separated by 20 μm) with each of the five dose rates R, obtained by attenuating the microfocused beam.

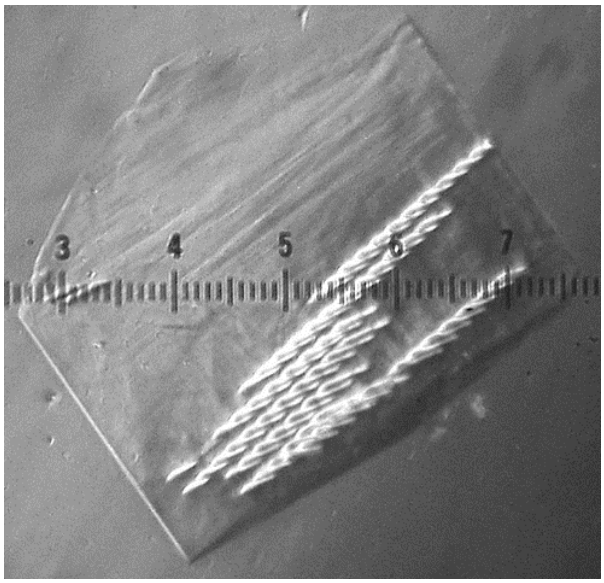

Figure S3 A thaumatin crystal, removed from the cryoloop, after microbeam irradiation following the general scheme illustrated in Figure S2. The major scale divisions are approximately 100 μm. The crystal was translated by 20 μm between measurement of each intensity versus dose frame set. Each position was irradiated using a different dose rate, but total exposure times varied such that all positions received the same dose, consistent with their similar appearances.

Figure S4 The flux density in the unattenuated beam generated optically visible fluorescence in the X-ray illuminated region at all temperatures. (Top) A lysozyme crystal at 260 K, with the beam hutch lights on (left) and off (right), as viewed through the beamline telescope. (Bottom) A lysozyme crystal at 100 K. The right-hand frame shows the fluorescence afterglow following six consecutive exposures separated by 1 s. At 260 K the fluorescence faded immediately, but at 100 K it persisted for ~6-8 seconds. Shape and brightness variations of the cylindrical illuminated crystal regions are due to reflection and refraction from crystal facets.

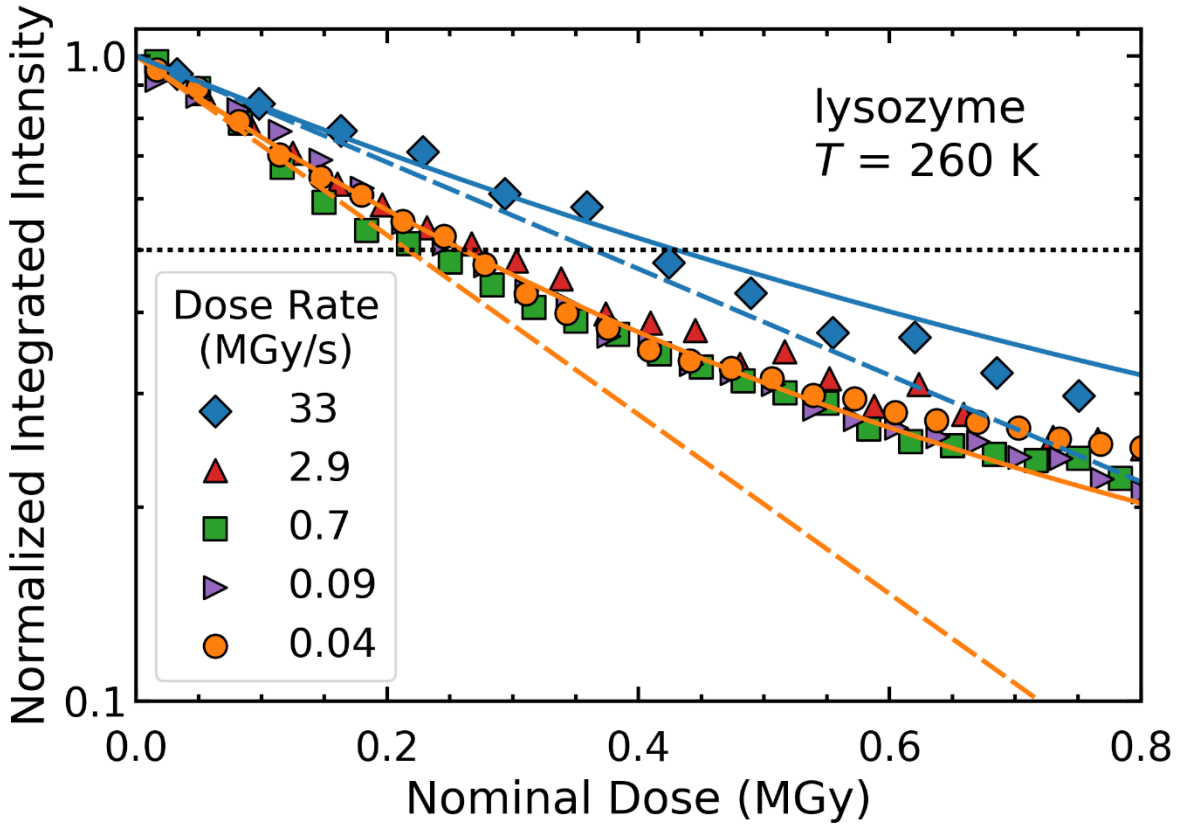

Figure S5 Representative semi-log plot of the integrated intensity in diffraction peaks versus dose at several dose rates, acquired from a single lysozyme crystal at 260 K; data at 300 K are shown in Fig. 1. The crystal was held in a fixed orientation and data for different dose rates was collected from five different positions. The intensity has an initial exponential decay (dashed lines), but varies much more gradually with dose at larger doses. At large doses/long times the data for different dose rates must converge. The solid lines are single-parameter fits to data at the highest and lowest dose rates based on the model described here. The intersection of the dotted black line with each dose curve determines the corresponding half-dose $D_{1/2}$. At 260 K the half-doses at all dose rates are larger than at 300 K. Doses and dose rates in all figures are averages within the area of the Gaussian beam's FWHM.

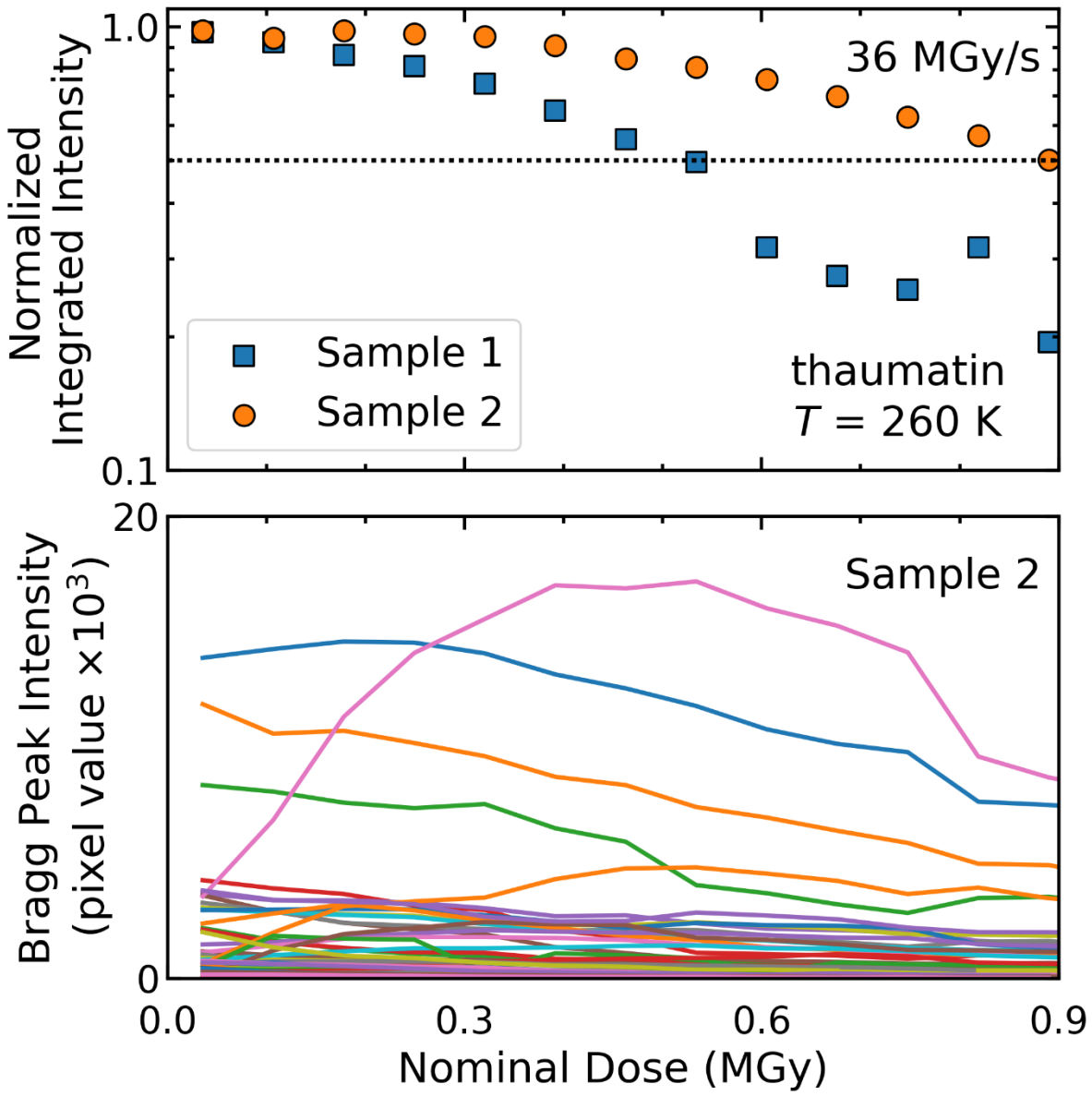

Figure S6 (Top) Representative intensity vs dose curves for two thaumatin crystals at 260 K for a nominal dose rate of 36 MGy/s. Each curve was recorded from one sample position. Sample 3 shows an intensity variation with dose as in Fig. 1, while Sample 4 exhibits an initial plateau in intensity. (Bottom) For samples and positions that yield plateaus or near plateaus in integrated intensity, a few to several diffraction peaks show a strong initial increase in intensity with dose, before decaying at larger doses. Similar data acquired at a dose rate of 0.09 MGy/s are shown in Fig. 2.

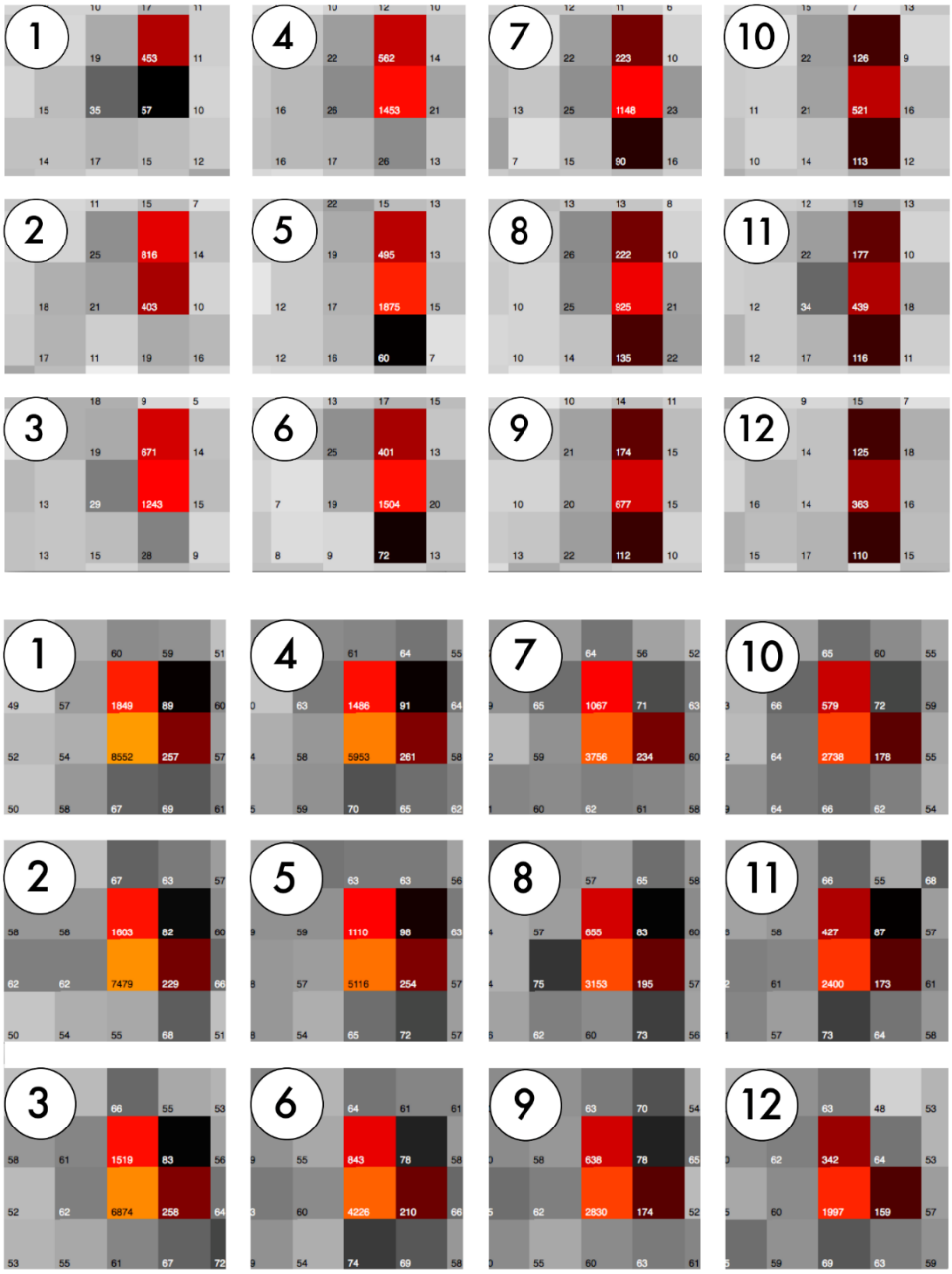

Figure S7 Examples of the evolution of peak intensity with dose, as indicated by detector pixel counts, for thaumatin crystals with a nominal incident dose rate of 36 MGy/s, a detector frame rate of 500 Hz, and a detector counting time of 1 ms. Large numbers in circles refer to detector frame numbers, and small numbers in the lower left corner of each pixel gives the photon count. The dose per frame is 71 kGy. (Top) A peak measured at T=260 K, which initially brightens with increasing dose before dimming at larger doses. (Bottom). A peak measured at T=300 K that monotonically dims with increasing dose.

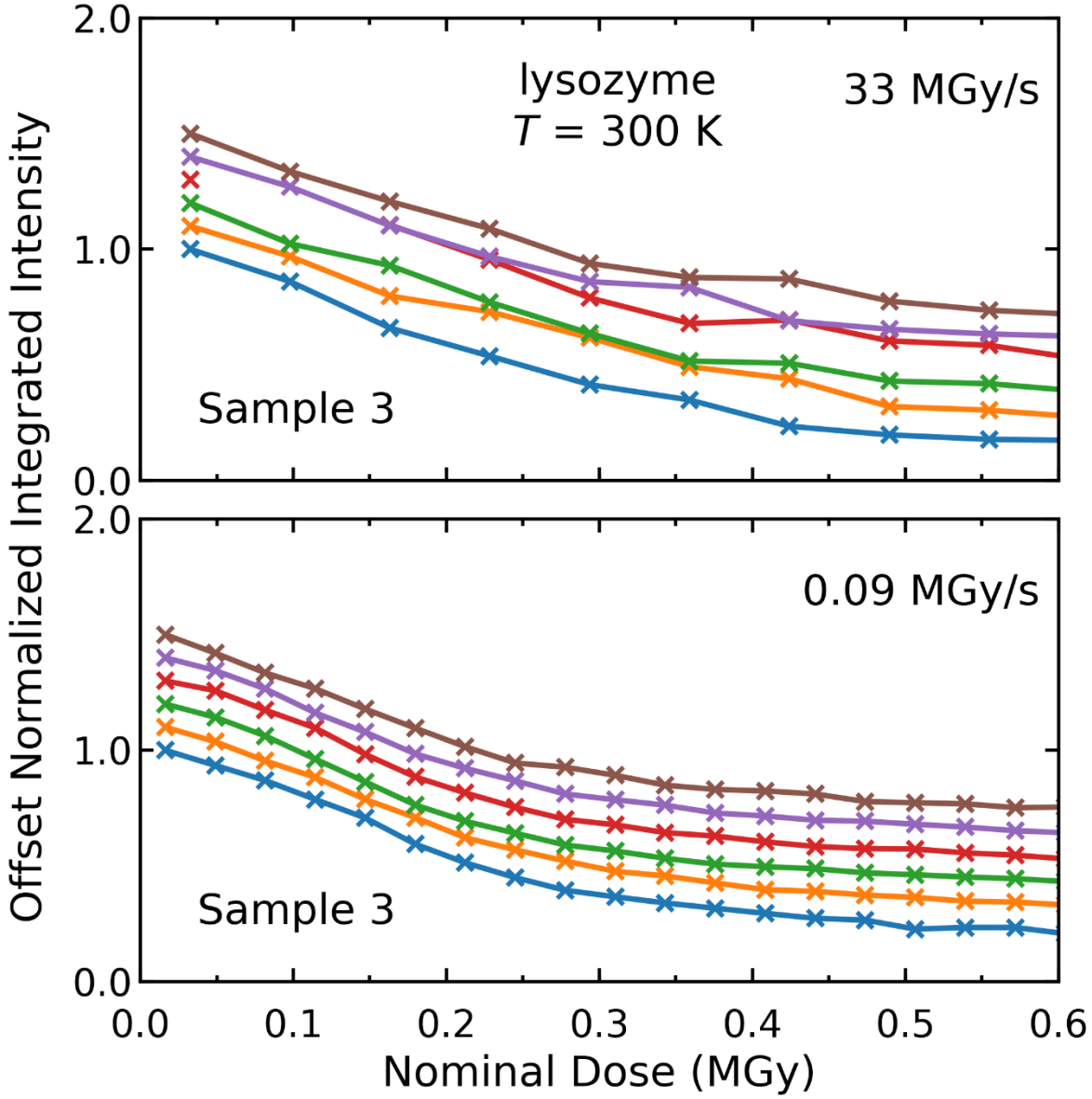

Figure S8 Comparison of integrated intensity versus dose data acquired at multiple positions on the same lysozyme sample at T=300 K, using (top) a 33 MGy/s dose rate and 500 Hz detector frame rate (0.066 MGy dose steps) and (bottom) using a 0.04 MGy/s dose rate and 1.2 Hz frame rate (0.033 MGy dose steps). At large dose rates, transient upward fluctuations in integrated intensity are observed for doses comparable to or larger than the half-dose.

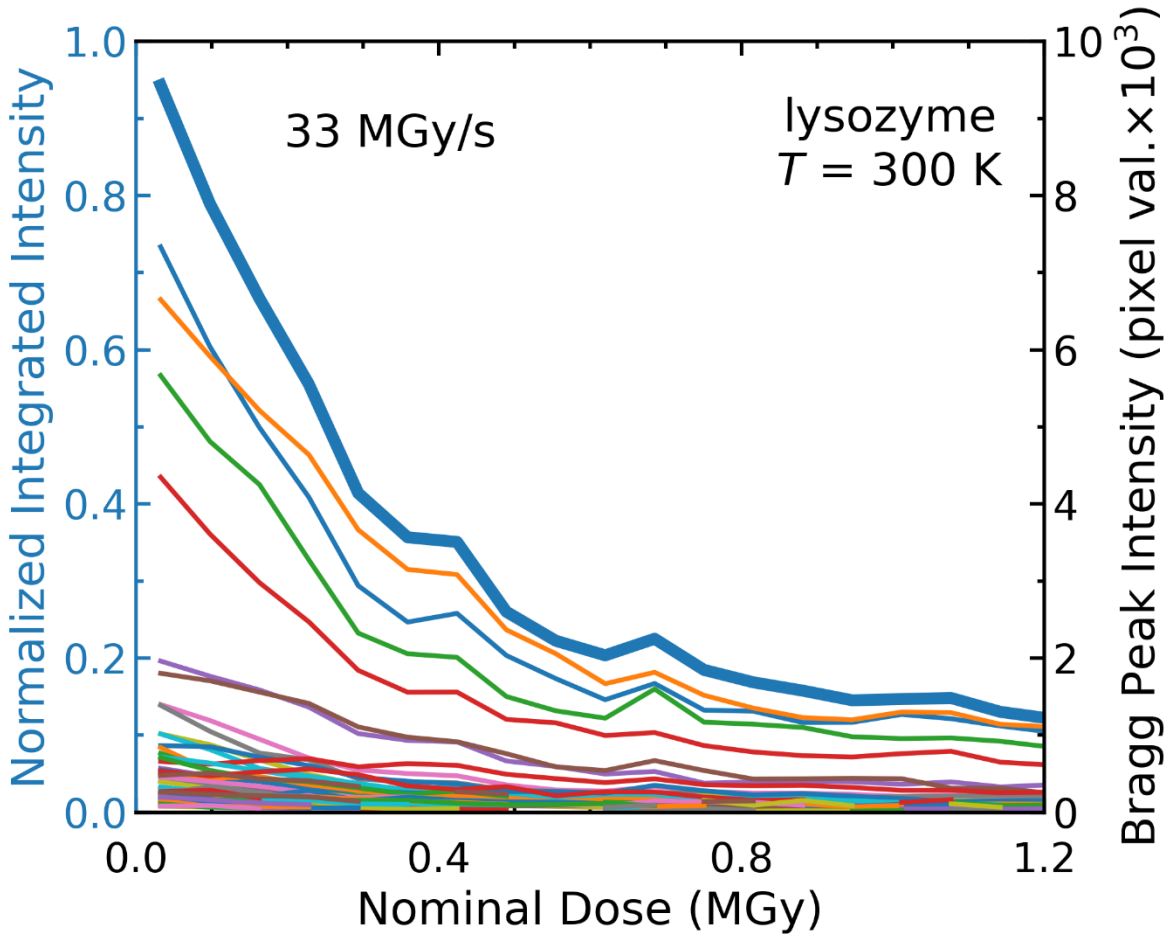

Figure S9 Plots of the integrated intensity (heavy blue line) and the intensity of individual Bragg peaks vs dose for the lysozyme crystal of Fig. S8 at T=300 K, for a dose rate of 33 MGy/s and a 500 Hz detector frame rate. Upward jumps in the integrated intensity correspond to jumps in the individual Bragg peak intensities, and have a duration of 2-4 ms.

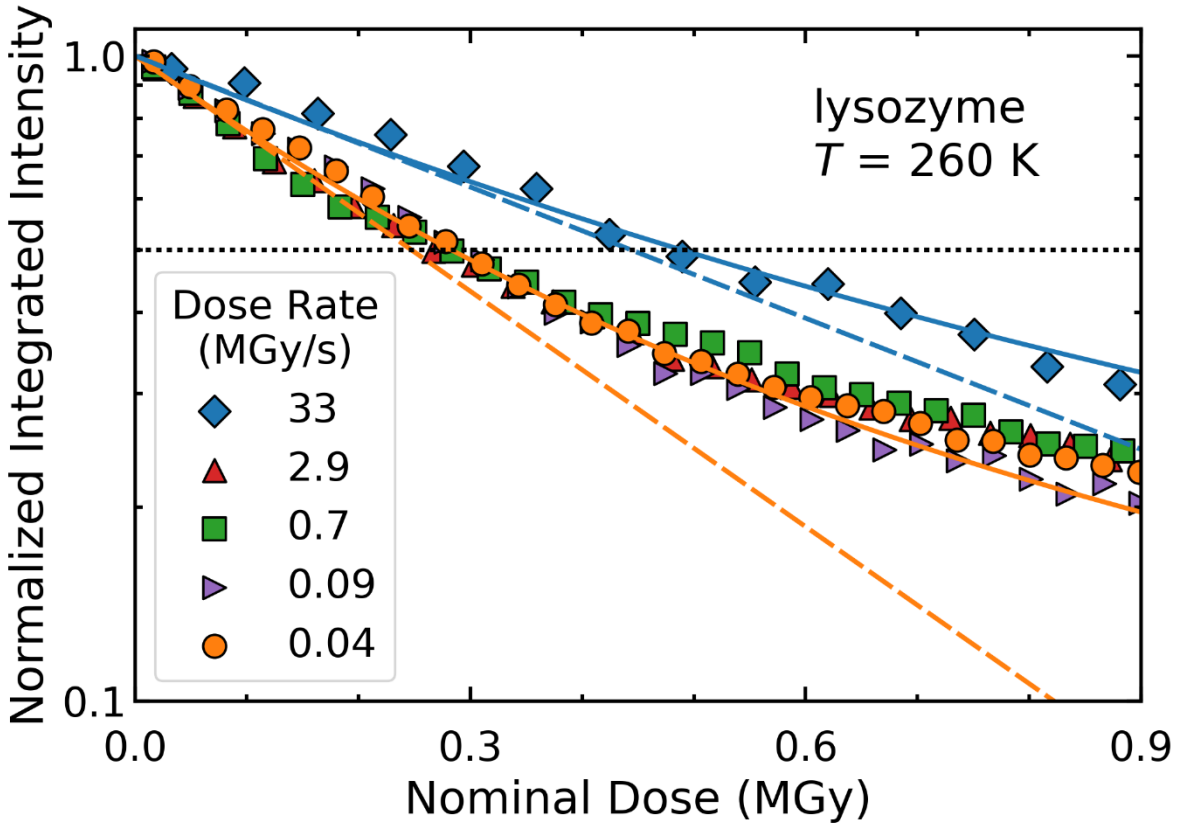

Figure S10 Representative semi-log plots of the integrated intensity in diffraction peaks versus dose at several dose rates, acquired from a single lysozyme crystal at 260 K, as in Figure S5, but as calculated by integrating the normalized peak intensities I/σ determined using XDS instead of the absolute intensities generated by DISTL.

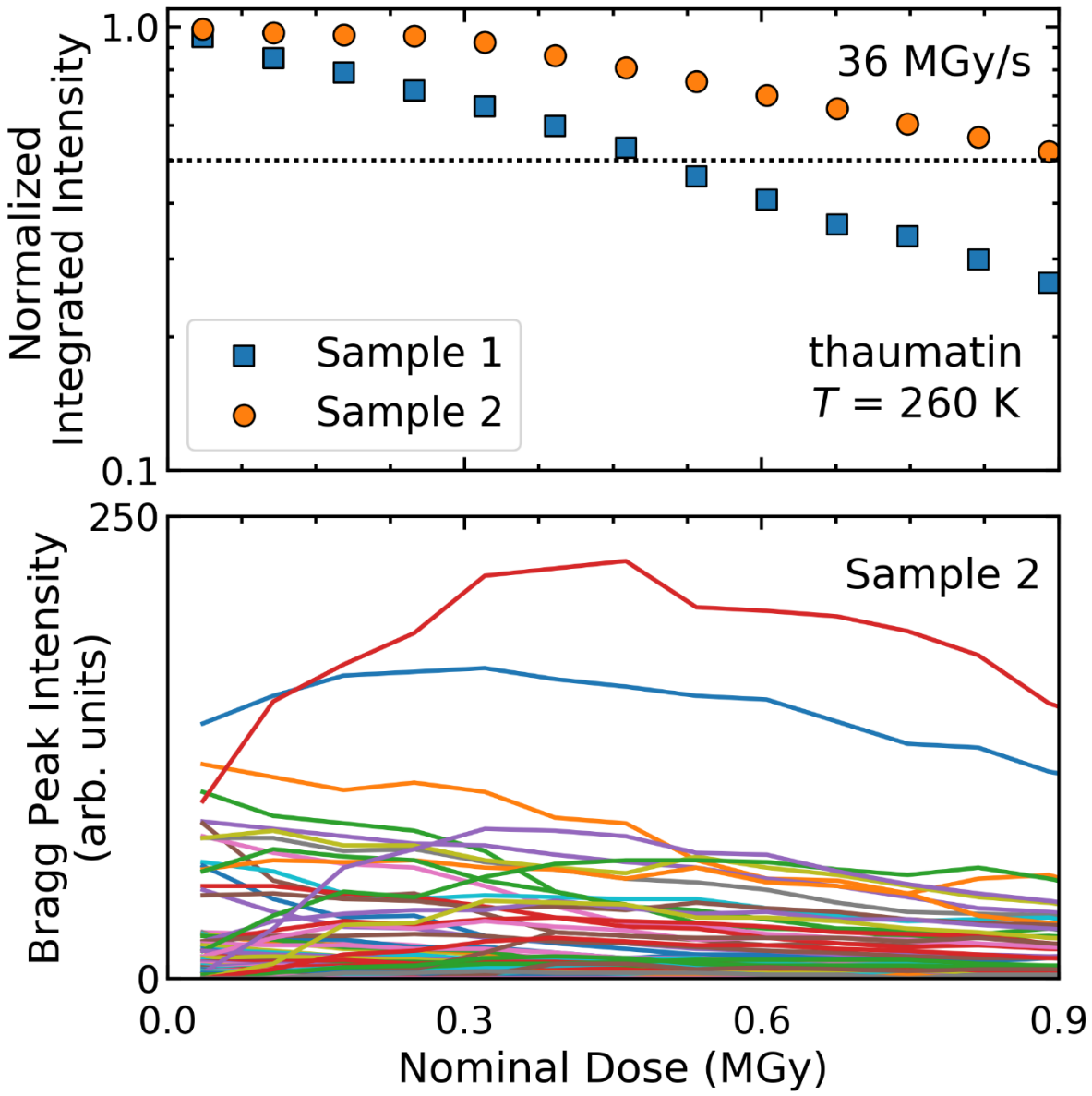

Figure S11 (Top) Representative integrated frame intensity vs dose curves for two thaumatin crystals at 260 K for a nominal dose rate of 36 MGy/s, as in Fig. S6 (top) but calculated using normalized individual peak intensities I/σ determined using XDS instead of the absolute background-subtracted intensities generated by DISTL. (Bottom) XDS-generated normalized peak intensities I/σ corresponding to the data in Fig. S6 (bottom).